

# Exploring Hilbert-Space Fragmentation on a Superconducting Processor

Yong-Yi Wang,<sup>1,2,\*</sup> Yun-Hao Shi,<sup>1,2,3,\*</sup> Zheng-Hang Sun,<sup>1,4,\*</sup> Chi-Tong Chen,<sup>1,2</sup> Zheng-An Wang,<sup>3,5</sup> Kui Zhao,<sup>3</sup> Hao-Tian Liu,<sup>1,2</sup> Wei-Guo Ma,<sup>1,2</sup> Ziting Wang,<sup>3</sup> Hao Li,<sup>3</sup> Jia-Chi Zhang,<sup>1,2</sup> Yu Liu,<sup>1,2</sup> Cheng-Lin Deng,<sup>1,2</sup> Tian-Ming Li,<sup>1,2</sup> Yang He,<sup>1,2</sup> Zheng-He Liu,<sup>1,2</sup> Zhen-Yu Peng,<sup>1,2</sup> Xiaohui Song,<sup>1,2</sup> Guangming Xue,<sup>3</sup> Haifeng Yu,<sup>3</sup> Kaixuan Huang,<sup>1,3,†</sup> Zhongcheng Xiang,<sup>1,2,‡</sup> Dongning Zheng,<sup>1,2,6,7</sup> Kai Xu,<sup>1,2,3,6,7,§</sup> and Heng Fan<sup>1,2,3,6,7,¶</sup>

<sup>1</sup>*Institute of Physics, Chinese Academy of Sciences, Beijing 100190, China*

<sup>2</sup>*School of Physical Sciences, University of Chinese Academy of Sciences, Beijing 100049, China*

<sup>3</sup>*Beijing Academy of Quantum Information Sciences, Beijing 100193, China*

<sup>4</sup>*Theoretical Physics III, Center for Electronic Correlations and Magnetism, Institute of Physics, University of Augsburg, D-86135 Augsburg, Germany*

<sup>5</sup>*Hefei National Laboratory, Hefei 230088, China*

<sup>6</sup>*Songshan Lake Materials Laboratory, Dongguan, Guangdong 523808, China*

<sup>7</sup>*CAS Center for Excellence in Topological Quantum Computation, UCAS, Beijing 100190, China, and Mozi Laboratory, Zhengzhou 450001, China*

Isolated interacting quantum systems generally thermalize, yet there are several counterexamples for the breakdown of ergodicity, such as many-body localization and quantum scars. Recently, ergodicity breaking has been observed in systems subjected to linear potentials, termed Stark many-body localization. This phenomenon is closely associated with Hilbert-space fragmentation, characterized by a strong dependence of dynamics on initial conditions. Here, we experimentally explore initial-state dependent dynamics using a ladder-type superconducting processor with up to 24 qubits, which enables precise control of the qubit frequency and initial state preparation. In systems with linear potentials, we observe distinct non-equilibrium dynamics for initial states with the same quantum numbers and energy, but with varying domain wall numbers. This distinction becomes increasingly pronounced as the system size grows, in contrast with disordered interacting systems. Our results provide convincing experimental evidence of the fragmentation in Stark systems, enriching our understanding of the weak breakdown of ergodicity.

*Introduction.*—In the past decades, the development of artificial quantum systems has motivated considerable studies of quantum statistical mechanics and non-equilibrium dynamics in many-body systems [1]. As a general framework for quantum thermalization, the eigenstate thermalization hypothesis (ETH) proposes that generic closed interacting systems thermalize under their own dynamics [2–4], while the breakdown of ergodicity can typically occur in interacting systems with strong disorder, known as many-body localization (MBL) [5–7]. Recent advances reveal intermediate behavior between the two extreme limits, referred to as weak ergodicity breaking, including phenomena such as quantum many-body scars [8–11] and Hilbert-space fragmentation (HSF) [12–18]. In weak ergodicity breaking systems, a small fraction of nonthermal eigenstates coexist within the majority of the thermal spectrum, allowing for halted thermalization under certain initial conditions [19].

As a prominent example of weak ergodicity breaking, HSF has been extensively explored theoretically in dipole-moment conserving systems, where the Hilbert space fragments into exponentially many disconnected Krylov subspaces due to the interplay between charge and dipole conservation, leading to the strong dependence of the dynamics on the initial conditions [12–14, 20]. On the other hand, systems subjected to a linear potential (hereinafter referred to as Stark systems) can also exhibit MBL-like behavior, such as long-lived initial state memory and multifractality, termed as Stark many-body localization (SMBL) [21–26]. Experimental studies of SMBL have been conducted using various experimental platforms [27–30]. In these systems subjected to a linear po-

tential, the emergence of dipole moment has raised questions and debates about its relationship with HSF [13, 23, 31–33]. A previous work showed a significant dependence of the dynamics on initial doublon fraction in the tilted one-dimensional Fermi-Hubbard model, but the initial conditions considered do not possess the same quantum numbers and energy [30]. Actually, the dynamics is profoundly related to the energy of chosen initial states even in disordered interacting systems, as a consequence of many-body mobility edge [34, 35]. Therefore, a direct demonstration of HSF in Stark systems requires a more thorough investigation into the dynamics for the initial states with the same quantum numbers and energy, excluding the potential influences stemming from different total charge and emergent dipole moment, as well as many-body mobility edges.

In this work, leveraging the precise control and flexibility of our ladder-type superconducting processor, we engineer the Hamiltonian and prepare various initial states with the same quantum numbers (charge and dipole moment) and energy for systems with up to 24 qubits. Applying site-dependent frequency deviations to individual qubits precisely, we observe distinct dynamical behavior in the Stark systems for initial states featuring varying domain wall numbers, even at a very small gradient. This phenomenon, in contrast to the conventional disorder-driven MBL, becomes increasingly pronounced as the system size grows. In addition, the efficient single-shot simultaneous readout enables us to experimentally measure the dynamics of participation entropy (PE) [35–37], which directly characterizes the available Hilbert space for a certain initial state. Contrary to the continuous growth of PE

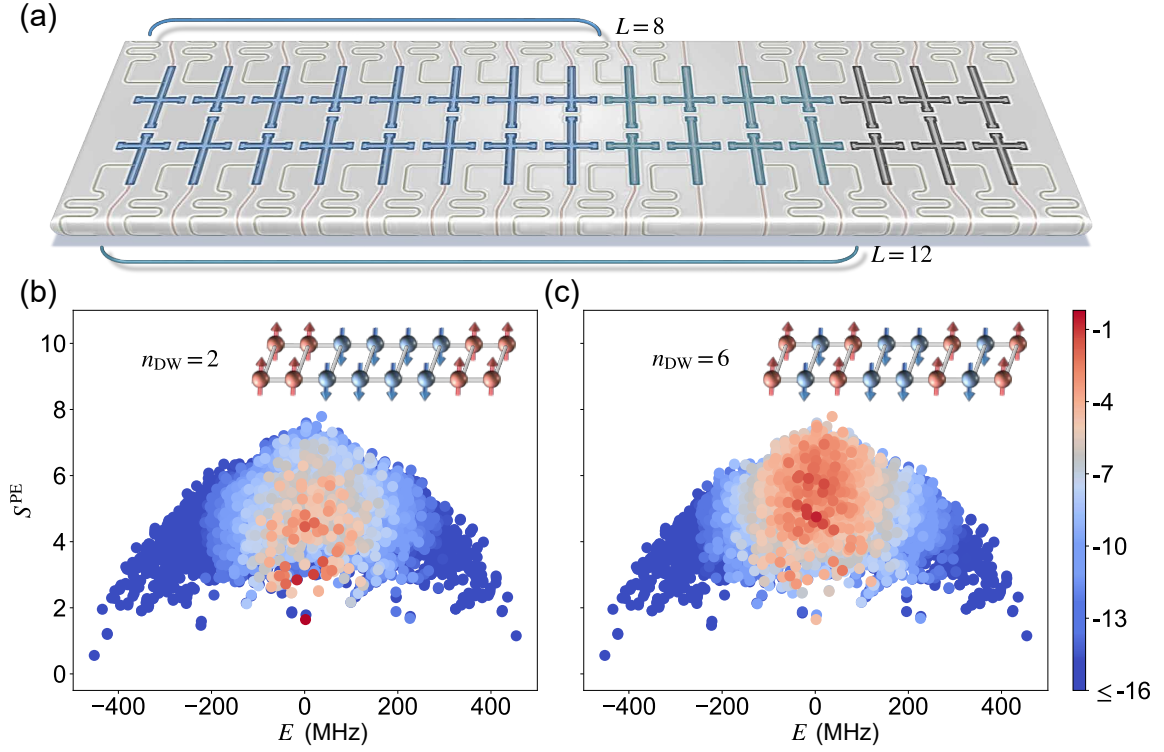


FIG. 1. Experimental setup. (a) Schematic representation of the ladder-type superconducting processor. For the experiment,  $L(8 \text{ \& } 12) \times 2$  qubits of the 30-qubit ladder are utilized, with nearest-neighboring  $\bar{J}_{\text{NN}}/2\pi \simeq 7$  MHz and next-nearest-neighboring couplings  $\bar{J}_{\text{NNN}} \lesssim \bar{J}_{\text{NN}}/6$ . (b), (c) Participation entropy of eigenstates for Hamiltonian [Eq. (1)] with  $\gamma = 4$ , colored by the logarithm of the eigenstate occupation numbers  $\log_{10} |\langle \psi_0 | E_n \rangle|^2$  for the initial state (b)  $|\psi_{n_{\text{DW}}=2}\rangle = |\mathbb{1}1000011\rangle$ , and (c)  $|\psi_{n_{\text{DW}}=6}\rangle = |\mathbb{1}0100101\rangle$ , with  $|0(\mathbb{1})\rangle$  denotes the ground (excited) state  $|0(1)\rangle$  on both legs of each ladder rung.

observed in systems subjected to a random potential, the limited growth of PE in systems subjected to a linear potential reveals that an initial state with a small domain wall number can only spread within a limited fraction of the Hilbert space, providing direct evidence of HSF in Stark systems.

*Model and set-up.*—Our experiments utilize a quantum processor equipped with a two-legged ladder structure consisting of 30 transmon qubits, as shown in Fig. 1(a). The effective Hamiltonian of the qubit-ladder processor reads [38–40]

$$\frac{\hat{H}}{\hbar} = \sum_{\langle jm; j'm' \rangle} J_{jm; j'm'} (\hat{\sigma}_{jm}^+ \hat{\sigma}_{j'm'}^- + \hat{\sigma}_{jm}^- \hat{\sigma}_{j'm'}^+) + \sum_{m=1,2} \sum_{j=1}^L W_{jm} \hat{\sigma}_{jm}^+ \hat{\sigma}_{jm}^-, \quad (1)$$

where  $\hbar = h/2\pi$  denotes the Planck constant,  $L$  is the length of the ladder,  $\hat{\sigma}_{jm}^+$  ( $\hat{\sigma}_{jm}^-$ ) is the two-level raising (lowering) operator for the qubit  $Q_{jm}$ . Here, the first summation runs over all nearest- and next-nearest-neighboring sites  $(j, m)$  and  $(j', m')$  with the averaged nearest-neighboring qubit-qubit coupling  $\bar{J}_{\text{NN}}/2\pi \simeq 7$  MHz and next-nearest-neighboring  $\bar{J}_{\text{NNN}} \lesssim \bar{J}_{\text{NN}}/6$  (see Supplementary Materials for coupling strengths in details). The on-site potential, denoted as  $W_{jm}$ , can be adjusted by applying fast flux bias to the Z control

lines of qubits. This flexibility enables the tuning of  $W_{jm}$  to both Stark (linear) potentials  $W_{jm}/\bar{J}_{\text{NN}} = -j\gamma$ , as well as random potentials  $W_{jm}/\bar{J}_{\text{NN}}$  drawn from a uniform distribution in  $[-W, W]$ , facilitating the quantum simulation of both SML and conventional MBL.

Utilizing a generalized form of Jordan-Wigner transformation [41, 42], the approximating ladder- $XX$  model can be mapped to an interacting spinless fermion model. As the gradient  $\gamma$  (or the disorder strength  $W$ ) increases, a transition from ergodicity to MBL exists in this typical nonintegrable model (see Supplementary Materials for details). One can expect that in the regime of a large gradient  $\gamma$ , the conservation of total  $U(1)$  charge  $\hat{Q} \equiv \sum_{j,m} \hat{\sigma}_{jm}^+ \hat{\sigma}_{jm}^-$ , together with the emergent conservation of dipole moment  $\hat{P} \equiv \sum_{j,m} j \hat{\sigma}_{jm}^+ \hat{\sigma}_{jm}^-$ , gives rise to HSF, so that the system would exhibit distinct dynamics with different initial states  $|\psi_0\rangle$ .

For  $|\psi_0\rangle$  considered in this work, the initial spin distribution is identical in the two rows of the ladder. These initial states share the same  $Q = \langle \hat{Q} \rangle$ ,  $P = \langle \hat{P} \rangle$ , and energy  $E = \langle \psi_0 | \hat{H} | \psi_0 \rangle$ , but vary in terms of total domain wall number, defined as  $n_{\text{DW}} = \sum_{j=1}^{L-1} (1 - \langle \hat{\sigma}_j^z \hat{\sigma}_{j+1}^z \rangle)/2$ , with  $\hat{\sigma}_j^z = (\hat{\sigma}_{j,1}^z + \hat{\sigma}_{j,2}^z)/2$ . Specifically, we examine two initial states for the system length  $L = 8$ :  $|\psi_{n_{\text{DW}}=2}\rangle = |\mathbb{1}1000011\rangle$  and  $|\psi_{n_{\text{DW}}=6}\rangle = |\mathbb{1}0100101\rangle$ , where  $|0(\mathbb{1})\rangle$  denotes the ground (excited) state of the single qubit  $|0(1)\rangle$  on both legs of each

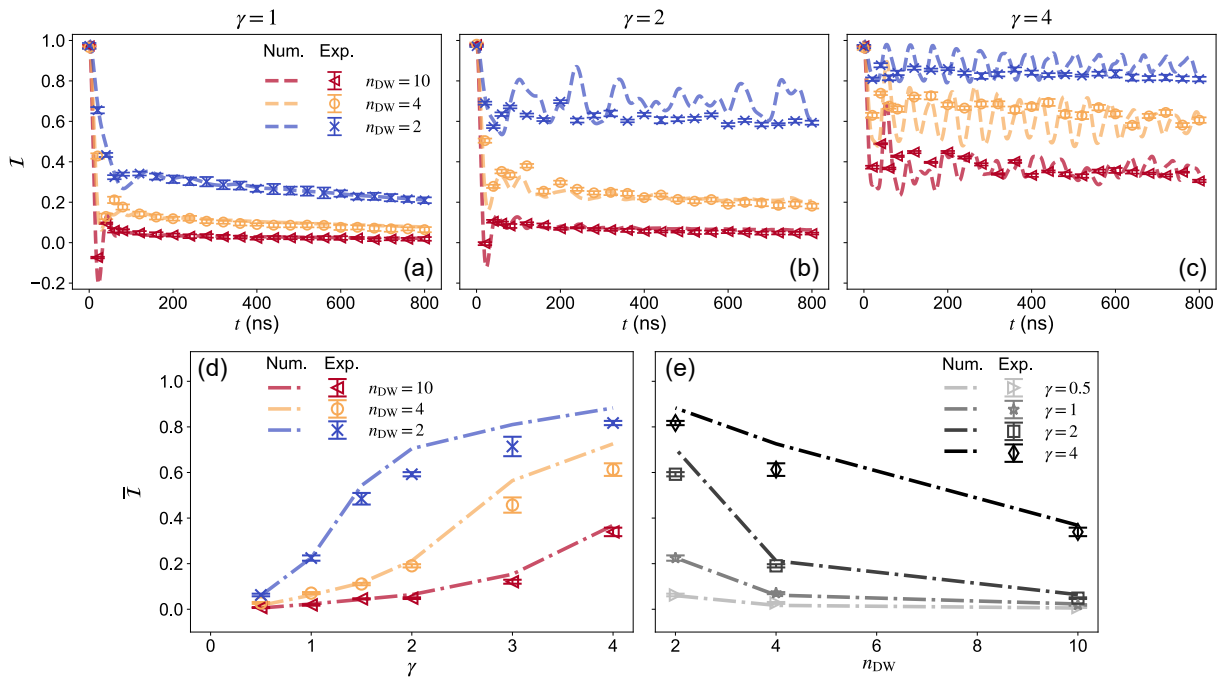


FIG. 2. Initial-state dependent dynamics of imbalance in the  $12 \times 2$  ladder. (a–c) The time evolution of the imbalance  $\mathcal{I}(t)$  for different initial states  $|\psi_{n_{\text{DW}}=2}\rangle = |1111000000111\rangle$ ,  $|\psi_{n_{\text{DW}}=4}\rangle = |110001100011\rangle$ , and  $|\psi_{n_{\text{DW}}=10}\rangle = |101010010101\rangle$  at gradients  $\gamma = 1, 2$  and  $4$ , respectively. Points are experimental data, each averaged over 5000 repetitions, and the dashed lines are numerical simulation. (d) The late-time averaged imbalance  $\bar{\mathcal{I}}$  as a function of the gradient  $\gamma$  for initial states with different domain wall numbers  $n_{\text{DW}}$ . (e) The late-time averaged imbalance  $\bar{\mathcal{I}}$  as a function of  $n_{\text{DW}}$  for different  $\gamma$ . Averages are taken over a time window from 600 to 800 ns. Error bars represent the standard deviation.

ladder rung (see the insets in Fig. 1(b) and (c)).

To quantify the localization in Hilbert space of spin configurations, we can calculate the PE of all eigenstates with exact diagonalization [35–37], defined as  $S^{\text{PE}}(n) = -\sum_i^{\mathcal{N}} p_i(n) \log p_i(n)$ , where  $\mathcal{N}$  is the dimension of Hilbert space, and  $p_i(n) = |\langle i|E_n\rangle|^2$  with  $\{|i\rangle\}$  being spin configuration basis (i.e.,  $\{\sigma^z\}$ ). Thus,  $S^{\text{PE}} = 0$  if the state is a single configuration, and  $S_{\text{GOE}}^{\text{PE}} = \log 0.482\mathcal{N}$  for Gaussian random states (see Supplementary Materials) [43]. In Fig. 1(b) and (c), the PE of eigenstates is displayed for the Hamiltonian [Eq. (1)] with a Stark potential at  $\gamma = 4$ . The colorbars represent the eigenstate occupation numbers  $|\langle \psi_0|E_n\rangle|^2$ , indicating the weight of eigenstate  $|E_n\rangle$  in the diagonal ensemble [2, 3], with respect to  $|\psi_0\rangle = |\psi_{n_{\text{DW}}=2}\rangle$  and  $|\psi_{n_{\text{DW}}=6}\rangle$ , respectively. Different from the ETH prediction, substantial fluctuations in PE are observed across the eigenstates within a narrow window around  $E = 0$ . Notably,  $|\psi_{n_{\text{DW}}=2}\rangle$  tends to predominantly overlap with a small number of eigenstates with relatively low PE, whereas the weight distribution for  $|\psi_{n_{\text{DW}}=6}\rangle$  spreads over a greater number of eigenstates with higher PE. This indicates that at  $\gamma = 4$ , these two states respectively reside within nearly disconnected fragments, with  $|\psi_{n_{\text{DW}}=2}\rangle$  more localized within a smaller fragment in the Hilbert space than  $|\psi_{n_{\text{DW}}=6}\rangle$ . The results for different  $\gamma$ , similar behavior in entanglement entropy, and the relation between the PE and domain wall numbers can be found in Supplementary Materials.

*Initial-state dependent dynamics.*—In contrast to ergodic dynamics, where memory of initial conditions is hidden in global operators, in MBL systems, memory of initial conditions can be preserved in local observables for generic high-energy initial states at long times after sudden quench [5–7]. To quantify the preservation of the information encoded in the initial state, we consider the imbalance generalized for any initial product state in the  $\{\sigma^z\}$  [28, 34, 44], defined as

$$\mathcal{I} = \frac{1}{2L} \sum_{jm} \langle \psi_0 | \hat{\sigma}_{jm}^z(t) \hat{\sigma}_{jm}^z(0) | \psi_0 \rangle. \quad (2)$$

The generalized imbalance will relax from initial value  $\mathcal{I} = 1$  to 0 if the system thermalizes, while it will maintain a finite value at long times if the system fails to thermalize.

To observe the initial-state dependent dynamics due to HSF, we consider three typical initial states for the system length  $L = 12$ , including  $|\psi_{n_{\text{DW}}=2}\rangle = |1111000000111\rangle$ ,  $|\psi_{n_{\text{DW}}=4}\rangle = |110001100011\rangle$ , and  $|\psi_{n_{\text{DW}}=10}\rangle = |101010010101\rangle$ . We prepare these initial states with the same quantum numbers and energy but different domain wall numbers, by simultaneously applying  $\pi$  pulses to half of the qubits. Calibrating the rectangular Z pulses for all qubits to create Stark potentials, we measure the generalized imbalance  $\mathcal{I}$  for different initial states following evolution over time  $t$ . The experimental data at  $\gamma = 1, 2$  and  $4$  are depicted in Fig. 2(a–c), along with numerical simulation (see Supplementary Materials for details).

We note that for  $\gamma = 1, 2$ , the average ratio of adjacent level spacings  $\langle r \rangle \gtrsim 0.5$ , close to prediction of Gaussian orthogonal ensemble, while  $\langle r \rangle \lesssim 0.4$  for  $\gamma = 4$ , exhibiting Poisson statistics (see Supplementary Materials) [35, 45, 46]. Therefore, at  $\gamma = 4$ , the imbalance oscillates around a finite value after a fast drop at short times for all three states, signifying a complete breakdown of ergodicity. At both  $\gamma = 1$  and 2, the imbalance for  $|\psi_0\rangle = |\psi_{n_{\text{DW}}=10}\rangle$  relaxes to zero, in accordance with ergodic dynamics. However, the relaxation gradually slows down as  $n_{\text{DW}}$  decreases. For  $\gamma = 2$ , the imbalance for  $|\psi_0\rangle = |\psi_{n_{\text{DW}}=2}\rangle$  has already exhibited pronounced oscillations around a value significantly above zero with negligible decay.

We then average the late-time imbalance over a time window from 600 to 800 ns, which is plotted against  $\gamma$  and  $n_{\text{DW}}$  in Fig. 2(d) and (e), respectively. On the one hand, the late-time imbalance for all initial states exhibits a clear upward trend as  $\gamma$  increases. On the other hand, we observe a monotonic decrease in the late-time imbalance as  $n_{\text{DW}}$  decreases. For initial states with smaller  $n_{\text{DW}}$ , the late-time imbalance displays a quicker rise as  $\gamma$  increases. By selecting initial states with identical quantum numbers and energy, the above experimental results demonstrate the initial-state dependent dynamics concerning domain wall numbers in Stark systems, which is a significant feature of HSF and weak breakdown of ergod-

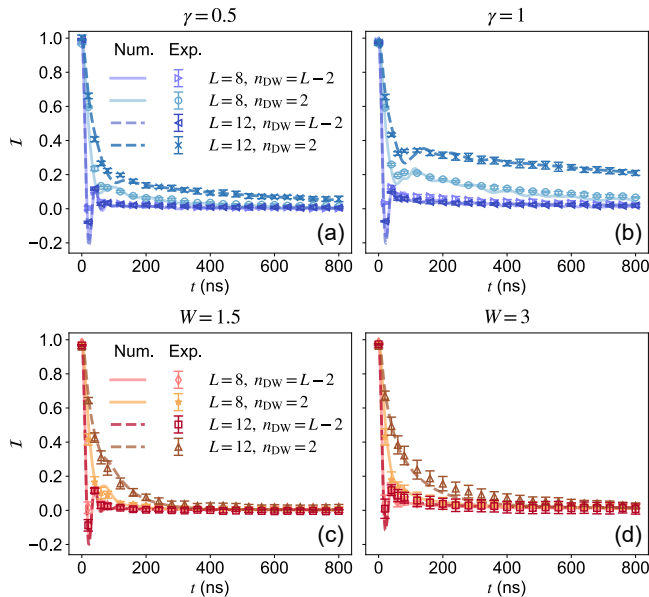


FIG. 3. Time evolution of imbalance for initial state  $|\psi_0\rangle = |\psi_{n_{\text{DW}}=2}\rangle$  and  $|\psi_{n_{\text{DW}}=L-2}\rangle$  in Stark systems with small gradients (a)  $\gamma = 0.5$  and (b) 1.5, as well as in disordered systems with disorder strengths (c)  $W = 1$  and (d) 3. The dependence of the imbalance on system size is depicted for  $L = 8$  and 12. In Stark systems (a, b), points are experimental data, each averaged over 5000 repetitions with error bars indicating the standard deviation. In disordered systems (c, d), the experimental data points are the average of 20 disorder realizations with 5000 repetitions for each realization, and the error bar shows the standard error of the mean. Lines represent numerical simulation.

icity.

*Comparison with disordered systems.*—According to the ETH, a fully delocalized regime exists in the disordered interacting systems with weak disorder, where the choice of the initial state is of no significance at long times [47, 48]. However, in terms of the ETH in its strong sense, numerical evidence has been put forward for the absence of an ETH-MBL transition in Stark systems due to HSF [31]. The question of whether HSF will lead to distinctions between Stark systems and disordered systems is a crucial aspect to explore. Here, we focus on Hamiltonian [Eq. (1)] with the gradients  $\gamma = 0.5$  and 1, and the disorder strengths  $W = 1.5$  and 3. For these parameters,  $\langle r \rangle$  remains close to 0.531, often viewed as a signature of ergodicity (see Supplementary Materials).

Considering the finite-size effects, we measure the generalized imbalance for  $|\psi_0\rangle = |\psi_{n_{\text{DW}}=2}\rangle$  and  $|\psi_{n_{\text{DW}}=L-2}\rangle$  with system lengths of  $L = 8$  and 12. The experimental data and numerical results are presented in Fig. 3. We can see that the imbalance for  $|\psi_0\rangle = |\psi_{n_{\text{DW}}=L-2}\rangle$  relaxes to zero in a short time for both Stark systems with  $\gamma = 0.5$  and 1 and disordered systems with  $W = 1.5$  and 3, irrespective of system size. However, in Fig. 3(a) and (b), an evident slowdown in relaxation can be observed for  $|\psi_0\rangle = |\psi_{n_{\text{DW}}=2}\rangle$  in Stark systems, which becomes more evident with increasing system size, even at a very small gradient  $\gamma = 0.5$ . A significantly higher late-time imbalance for  $L = 12$  compared to  $L = 8$  suggests a nonvanishing imbalance for systems with a sufficiently large size.

In contrast, as shown in Fig. 3(c) and (d), we can merely observe a slightly slower thermalization for  $|\psi_0\rangle = |\psi_{n_{\text{DW}}=2}\rangle$  compared to  $|\psi_{n_{\text{DW}}=L-2}\rangle$ , with the disorder-average imbalance approaching zero at long times for both initial states. Notably, these results remain consistent regardless of the system's increasing length, which starkly contrasts with the observation in Stark systems. The contrast unveils distinct mechanisms of localization between SMBL and conventional MBL.

*Dynamical signature of HSF via participation entropy.*—As discussed above, the Hilbert space tends to fragment into many disconnected Krylov subspaces with different dimensions in Stark systems. A direct quantity reflecting the extent to which a time-evolved state  $|\psi(t)\rangle$  spreads over the Hilbert space [34, 49] is the dynamical PE, defined as

$$S^{\text{PE}}(t) = - \sum_i^{\mathcal{N}} p_i(t) \log p_i(t), \quad (3)$$

with the multiqubit probabilities  $p_i(t) = |\langle \psi(t) | i \rangle|^2$ . For ergodic dynamics, the dynamical PE increases from  $S^{\text{PE}}(0) = 0$  for any initial product state to the late-time value  $S_{\text{GUE}}^{\text{PE}} = \log N - 1 + \gamma_e$  (with  $\gamma_e$  Euler's constant), as predicted by the Gaussian unitary ensemble (see Supplementary Materials) [50]. The dynamical PE determined by the multiqubit probabilities can be observed with our superconducting processor thanks to its efficient multiqubit simultaneous readout capability. Applying a Stark potential with  $\gamma = 2$  and a random potential with  $W = 4$  to the system, we track the time evolution of the multiqubit probabilities with site-resolved simultaneous readout at different times  $t$ . For the calculation



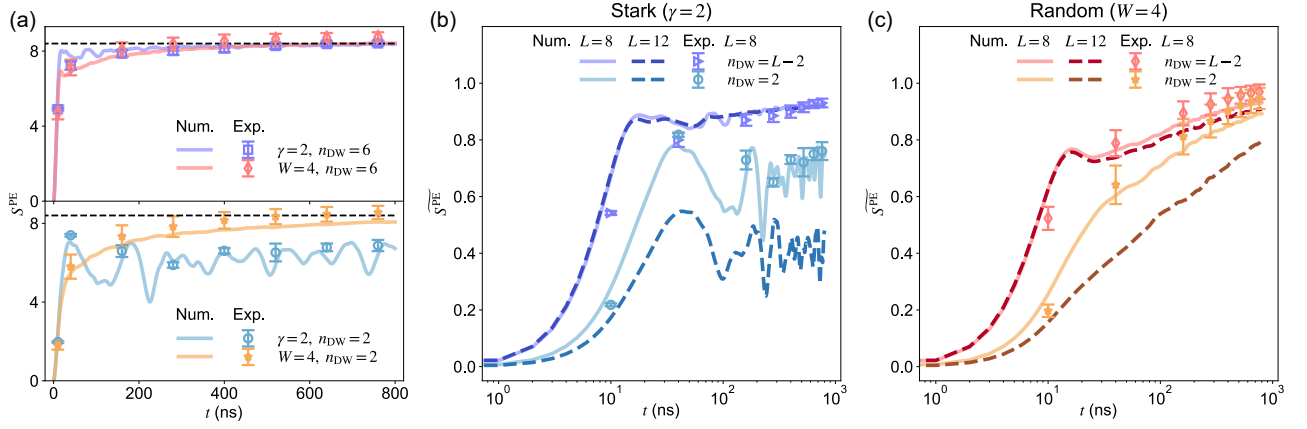


FIG. 4. Time evolution of participation entropy. (a) Dynamical participation entropy in the Stark system with  $\gamma = 2$  and the disordered system with  $W = 4$  for different initial states  $|\psi_0\rangle = |\psi_{n_{\text{DW}}=6}\rangle$  (upper panel) and  $|\psi_0\rangle = |\psi_{n_{\text{DW}}=2}\rangle$  (lower panel) with the system length  $L = 8$ . For  $|\psi_0\rangle = |\psi_{n_{\text{DW}}=6}\rangle$ , the numerical results of the late-time  $S^{\text{PE}}$  is around 8.4 in both systems, marked by the horizontal dashed lines in both panels. (b, c) Normalized PE  $\overline{S^{\text{PE}}} = S^{\text{PE}}/S_{\text{GUE}}^{\text{PE}}$  with the same experimental data as (a) against the logarithm of time, in (b) the Stark system with  $\gamma = 2$  and (c) the disordered system with  $W = 4$ . Numerical results are depicted by lines for  $L = 8$  and 12. The experimental data for  $S^{\text{PE}}$  in Stark systems are obtained from five sets of independent experiments, each consisting of 500,000 repeated single-shot measurements. For disordered systems, data are from 20 disorder realizations, each with 500,000 measurements. Error bars indicate the standard deviation.

of the PE, the experimental data of the multiqubit probabilities in Fig. 4 are obtained from 500,000 repeated measurements and post-selected within the  $Q = L$  sector. As shown in Fig. 4(a), the initial product states, as Fock states, gradually propagate and cover the available Hilbert space at long times, reflected by the increase of PE. For both models, dynamics for  $|\psi_0\rangle = |\psi_{n_{\text{DW}}=6}\rangle$  approaches similar values of PE at long times. However, in a random potential, the PE for  $|\psi_0\rangle = |\psi_{n_{\text{DW}}=2}\rangle$  increases and eventually approaches the late-time value for  $|\psi_{n_{\text{DW}}=6}\rangle$  (marked by dashed lines in Fig. 4(a)), while in a Stark potential, it oscillates at a lower value, suggesting that  $|\psi_{n_{\text{DW}}=2}\rangle$  can only propagate in a restricted fraction of the Hilbert space.

In Fig. 4(b) and (c), we plot the experimental data of normalized PE  $\overline{S^{\text{PE}}} = S^{\text{PE}}/S_{\text{GUE}}^{\text{PE}}$  against the logarithm of time, with numerical results for  $L = 12$ , in systems with a Stark and a random potential, respectively. In Stark systems, we observe that the data of normalized PE for  $|\psi_{n_{\text{DW}}=L-2}\rangle$  nearly coincide for different system sizes, while those for  $|\psi_{n_{\text{DW}}=2}\rangle$  decreases with the increasing system size. This indicates that  $|\psi_{n_{\text{DW}}=L-2}\rangle$  can spread in a fraction of Hilbert space whose dimension scales with the size of the entire Hilbert space, while the dimension of Krylov subspace corresponding to  $|\psi_{n_{\text{DW}}=2}\rangle$  becomes vanishingly small in the thermodynamic limit (see Supplementary Materials for further discussion). In contrast, in disordered systems,  $\overline{S^{\text{PE}}}$  exhibits unceasing growth within the experimental time for both initial states, despite differences in relaxation. The comparison to disordered interacting systems further reveals a distinctive characteristic in Stark systems, where the initial-state dependent dynamics is closely associated with disconnected Krylov subspaces with different scaling behaviors.

*Conclusions and outlook.*—In summary, we have reported

the experimental observation of distinctively initial-state dependent dynamics in Stark systems, by studying the dynamics of imbalance and PE for initial states with varying domain wall numbers with system sizes up to  $12 \times 2$ . This experiment elucidates the crucial distinctions between SMBL and disorder-driven MBL, which we attribute to the HSF mechanism. Moreover, the close relation between the late-time imbalance and domain wall numbers of initial states indicates the presence of a more intricate landscape of the mobility edge in weak ergodicity-breaking systems like Stark systems [51, 52], in contrast with disorder-driven MBL where mobility edge relies solely on energy [34].

The efficient readout of our superconducting processor enables the measurement of PE, offering direct evidence of HSF. However, it is a challenging experimental task for systems with a length of 12 or larger. To this end, the development of scalable experimental probes for HSF is a crucial task for the future, as it will facilitate further systematic investigations of HSF in Stark or other higher-dimensional weak ergodicity-breaking systems [53, 54].

This work was supported by the National Natural Science Foundation of China (Grants Nos. 92265207, T2121001, 11904393, 92065114, 11875220, and 12047502), Innovation Program for Quantum Science and Technology (Grant No. 2-6), Strategic Priority Research Program of Chinese Academy of Sciences (Grant No. XDB28000000), Beijing Natural Science Foundation (Grant No. Z200009), Scientific Instrument Developing Project of Chinese Academy of Sciences (Grant No. YJKYYQ20200041), the Key-Area Research and Development Program of Guang-Dong Province (Grant Nos. 2018B030326001 and 2020B0303030001) and the State Key Development Program for Basic Research of China (Grant No. 2017YFA0304300).

\* These authors contributed equally to this work.

† [huangkx@baqis.ac.cn](mailto:huangkx@baqis.ac.cn)

‡ [zcxiaang@iphy.ac.cn](mailto:zcxiaang@iphy.ac.cn)

§ [kaixu@iphy.ac.cn](mailto:kaixu@iphy.ac.cn)

¶ [hfan@iphy.ac.cn](mailto:hfan@iphy.ac.cn)

- [1] I. M. Georgescu, S. Ashhab, and F. Nori, Quantum simulation, *Rev. Mod. Phys.* **86**, 153 (2014).
- [2] M. Rigol, V. Dunjko, and M. Olshanii, Thermalization and its mechanism for generic isolated quantum systems, *Nature* **452**, 854 (2008).
- [3] L. D'Alessio, Y. Kafri, A. Polkovnikov, and M. Rigol, From quantum chaos and eigenstate thermalization to statistical mechanics and thermodynamics, *Adv. Phys.* **65**, 239 (2016).
- [4] J. M. Deutsch, Eigenstate thermalization hypothesis, *Reports Prog. Phys.* **81**, 082001 (2018).
- [5] R. Nandkishore and D. A. Huse, Many-Body Localization and Thermalization in Quantum Statistical Mechanics, *Annu. Rev. Condens. Matter Phys.* **6**, 15 (2015).
- [6] E. Altman, Many-body localization and quantum thermalization, *Nat. Phys.* **14**, 979 (2018).
- [7] D. A. Abanin, E. Altman, I. Bloch, and M. Serbyn, Colloquium: Many-body localization, thermalization, and entanglement, *Rev. Mod. Phys.* **91**, 21001 (2019).
- [8] H. Bernien, S. Schwartz, A. Keesling, H. Levine, A. Omran, H. Pichler, S. Choi, A. S. Zibrov, M. Endres, M. Greiner, V. Vuletic, and M. D. Lukin, Probing many-body dynamics on a 51-atom quantum simulator, *Nature* **551**, 579 (2017).
- [9] C. J. Turner, A. A. Michailidis, D. A. Abanin, M. Serbyn, and Z. Papić, Weak ergodicity breaking from quantum many-body scars, *Nat. Phys.* **14**, 745 (2018).
- [10] M. Serbyn, D. A. Abanin, and Z. Papić, Quantum many-body scars and weak breaking of ergodicity, *Nat. Phys.* **17**, 675 (2021).
- [11] P. Zhang, H. Dong, Y. Gao, L. Zhao, J. Hao, J. Y. Desaulles, Q. Guo, J. Chen, J. Deng, B. Liu, W. Ren, Y. Yao, X. Zhang, S. Xu, K. Wang, F. Jin, X. Zhu, B. Zhang, H. Li, C. Song, Z. Wang, F. Liu, Z. Papić, L. Ying, H. Wang, and Y. C. Lai, Many-body Hilbert space scarring on a superconducting processor, *Nat. Phys.* **19**, 120 (2023).
- [12] P. Sala, T. Rakovszky, R. Verresen, M. Knap, and F. Pollmann, Ergodicity Breaking Arising from Hilbert Space Fragmentation in Dipole-Conserving Hamiltonians, *Phys. Rev. X* **10**, 011047 (2020).
- [13] V. Khemani, M. Hermele, and R. Nandkishore, Localization from Hilbert space shattering: From theory to physical realizations, *Phys. Rev. B* **101**, 174204 (2020).
- [14] L. Herviou, J. H. Bardarson, and N. Regnault, Many-body localization in a fragmented Hilbert space, *Phys. Rev. B* **103**, 134207 (2021).
- [15] Z. C. Yang, F. Liu, A. V. Gorshkov, and T. Iadecola, Hilbert-Space Fragmentation from Strict Confinement, *Phys. Rev. Lett.* **124**, 207602 (2020).
- [16] D. Hahn, P. A. McClarty, and D. J. Luitz, Information dynamics in a model with Hilbert space fragmentation, *SciPost Phys.* **11**, 074 (2021).
- [17] S. Moudgalya, A. Prem, R. Nandkishore, N. Regnault, and B. A. Bernevig, Thermalization and its absence within krylov subspaces of a constrained hamiltonian, in *Memorial Volume for Shoucheng Zhang* (2021) Chap. 7, pp. 147–209.
- [18] S. Moudgalya and O. I. Motrunich, Hilbert Space Fragmentation and Commutant Algebras, *Phys. Rev. X* **12**, 011050 (2022).
- [19] S. Moudgalya, B. A. Bernevig, and N. Regnault, Quantum many-body scars and Hilbert space fragmentation: a review of exact results, *Reports Prog. Phys.* **85**, 086501 (2022).
- [20] S. Pai, M. Pretko, and R. M. Nandkishore, Localization in Fractional Random Circuits, *Phys. Rev. X* **9**, 021003 (2019).
- [21] M. Schulz, C. A. Hooley, R. Moessner, and F. Pollmann, Stark Many-Body Localization, *Phys. Rev. Lett.* **122**, 040606 (2019).
- [22] E. van Nieuwenburg, Y. Baum, and G. Refael, From Bloch oscillations to many-body localization in clean interacting systems, *Proc. Natl. Acad. Sci.* **116**, 9269 (2019).
- [23] S. R. Taylor, M. Schulz, F. Pollmann, and R. Moessner, Experimental probes of Stark many-body localization, *Phys. Rev. B* **102**, 054206 (2020).
- [24] R. Yao and J. Zakrzewski, Many-body localization of bosons in an optical lattice: Dynamics in disorder-free potentials, *Phys. Rev. B* **102**, 104203 (2020).
- [25] Y.-Y. Wang, Z.-H. Sun, and H. Fan, Stark many-body localization transitions in superconducting circuits, *Phys. Rev. B* **104**, 205122 (2021).
- [26] G. Zisling, D. M. Kennes, and Y. Bar Lev, Transport in Stark many-body localized systems, *Phys. Rev. B* **105**, L140201 (2022).
- [27] W. Morong, F. Liu, P. Becker, K. S. Collins, L. Feng, A. Kyprianidis, G. Pagano, T. You, A. V. Gorshkov, and C. Monroe, Observation of Stark many-body localization without disorder, *Nature* **599**, 393 (2021).
- [28] Q. Guo, C. Cheng, H. Li, S. Xu, P. Zhang, Z. Wang, C. Song, W. Liu, W. Ren, H. Dong, R. Mondaini, and H. Wang, Stark Many-Body Localization on a Superconducting Quantum Processor, *Phys. Rev. Lett.* **127**, 240502 (2021).
- [29] S. Scherg, T. Kohlert, P. Sala, F. Pollmann, B. Hebbe Madhusudhana, I. Bloch, and M. Aidelsburger, Observing non-ergodicity due to kinetic constraints in tilted Fermi-Hubbard chains, *Nat. Commun.* **12**, 4490 (2021).
- [30] T. Kohlert, S. Scherg, P. Sala, F. Pollmann, B. Hebbe Madhusudhana, I. Bloch, and M. Aidelsburger, Exploring the Regime of Fragmentation in Strongly Tilted Fermi-Hubbard Chains, *Phys. Rev. Lett.* **130**, 010201 (2023).
- [31] E. V. Doggen, I. V. Gornyi, and D. G. Polyakov, Stark many-body localization: Evidence for Hilbert-space shattering, *Phys. Rev. B* **103**, 100202 (2021).
- [32] R. Yao, T. Chanda, and J. Zakrzewski, Nonergodic dynamics in disorder-free potentials, *Ann. Phys.* **435**, 168540 (2021).
- [33] E. V. Doggen, I. V. Gornyi, and D. G. Polyakov, Many-body localization in a tilted potential in two dimensions, *Phys. Rev. B* **105**, 134204 (2022).
- [34] Q. Guo, C. Cheng, Z.-H. Sun, Z. Song, H. Li, Z. Wang, W. Ren, H. Dong, D. Zheng, Y.-r. Zhang, R. Mondaini, H. Fan, and H. Wang, Observation of energy-resolved many-body localization, *Nat. Phys.* **17**, 234 (2021).
- [35] D. J. Luitz, N. Laflorencie, and F. Alet, Many-body localization edge in the random-field Heisenberg chain, *Phys. Rev. B* **91**, 081103(R) (2015).
- [36] D. J. Luitz, F. Alet, and N. Laflorencie, Universal Behavior beyond Multifractality in Quantum Many-Body Systems, *Phys. Rev. Lett.* **112**, 057203 (2014).
- [37] N. Macé, F. Alet, and N. Laflorencie, Multifractal Scalings Across the Many-Body Localization Transition, *Phys. Rev. Lett.* **123**, 180601 (2019).
- [38] Q. Zhu, Z.-H. Sun, M. Gong, F. Chen, Y.-R. Zhang, Y. Wu, Y. Ye, C. Zha, S. Li, S. Guo, H. Qian, H.-L. Huang, J. Yu, H. Deng, H. Rong, J. Lin, Y. Xu, L. Sun, C. Guo, N. Li, F. Liang, C.-Z. Peng, H. Fan, X. Zhu, and J.-W. Pan, Observation of Thermalization and Information Scrambling in a Super-

- conducting Quantum Processor, [Phys. Rev. Lett. \*\*128\*\*, 160502 \(2022\)](#).
- [39] Z.-C. Xiang, K. Huang, Y.-R. Zhang, T. Liu, Y.-H. Shi, C.-L. Deng, T. Liu, H. Li, G.-H. Liang, Z.-Y. Mei, H. Yu, G. Xue, Y. Tian, X. Song, Z.-B. Liu, K. Xu, D. Zheng, F. Nori, and H. Fan, Simulating Chern insulators on a superconducting quantum processor, [Nat. Commun. \*\*14\*\*, 5433 \(2023\)](#).
- [40] Y.-H. Shi, Z.-H. Sun, Y.-Y. Wang, Z.-A. Wang, Y.-R. Zhang, W.-G. Ma, H.-T. Liu, K. Zhao, J.-C. Song, G.-H. Liang, Z.-Y. Mei, J.-C. Zhang, H. Li, C.-T. Chen, X. Song, J. Wang, G. Xue, H. Yu, K. Huang, Z. Xiang, K. Xu, D. Zheng, and H. Fan, Probing spin hydrodynamics on a superconducting quantum simulator, [arXiv:2310.06565](#).
- [41] S. P. Strong and A. J. Millis, Competition between singlet formation and magnetic ordering in one-dimensional spin systems, [Phys. Rev. Lett. \*\*69\*\*, 2419 \(1992\)](#).
- [42] M. Azzouz, L. Chen, and S. Moukouri, Calculation of the singlet-triplet gap of the antiferromagnetic Heisenberg model on a ladder, [Phys. Rev. B \*\*50\*\*, 6233 \(1994\)](#).
- [43] E. J. Torres-Herrera, J. Karp, M. Távora, and L. F. Santos, Realistic many-body quantum systems vs. full random matrices: Static and dynamical properties, [Entropy \*\*18\*\*, 359 \(2016\)](#).
- [44] M. Schreiber, S. S. Hodgman, P. Bordia, H. P. Lüschen, M. H. Fischer, R. Vosk, E. Altman, U. Schneider, and I. Bloch, Observation of many-body localization of interacting fermions in a quasirandom optical lattice, [Science \*\*349\*\*, 842 \(2015\)](#).
- [45] Y. Y. Atas, E. Bogomolny, O. Giraud, and G. Roux, Distribution of the ratio of consecutive level spacings in random matrix ensembles, [Phys. Rev. Lett. \*\*110\*\*, 084101 \(2013\)](#).
- [46] P. Roushan, C. Neill, J. Tangpanitanon, V. M. Bastidas, A. Megrant, R. Barends, Y. Chen, Z. Chen, B. Chiaro, A. Dunsworth, A. Fowler, B. Foxen, M. Giustina, E. Jeffrey, J. Kelly, E. Lucero, J. Mutus, M. Neeley, C. Quintana, D. Sank, A. Vainsencher, J. Wenner, T. White, H. Neven, D. G. Angelakis, and J. Martinis, Spectroscopic signatures of localization with interacting photons in superconducting qubits, [Science \*\*358\*\*, 1175 \(2017\)](#).
- [47] J. Hauschild, F. Heidrich-Meisner, and F. Pollmann, Domain-wall melting as a probe of many-body localization, [Phys. Rev. B \*\*94\*\*, 161109\(R\) \(2016\)](#).
- [48] Y. Prasad and A. Garg, Initial state dependent dynamics across the many-body localization transition, [Phys. Rev. B \*\*105\*\*, 214202 \(2022\)](#).
- [49] H. Li, Y.-Y. Wang, Y.-H. Shi, K. Huang, X. Song, G.-H. Liang, Z.-Y. Mei, B. Zhou, H. Zhang, J.-C. Zhang, S. Chen, S. P. Zhao, Y. Tian, Z.-Y. Yang, Z. Xiang, K. Xu, D. Zheng, and H. Fan, Observation of critical phase transition in a generalized Aubry-André-Harper model with superconducting circuits, [npj Quantum Inf. \*\*9\*\*, 40 \(2023\)](#).
- [50] S. Boixo, S. V. Isakov, V. N. Smelyanskiy, R. Babbush, N. Ding, Z. Jiang, M. J. Bremner, J. M. Martinis, and H. Neven, Characterizing quantum supremacy in near-term devices, [Nat. Phys. \*\*14\*\*, 595 \(2018\)](#).
- [51] L. Zhang, Y. Ke, W. Liu, and C. Lee, Mobility edge of Stark many-body localization, [Phys. Rev. A \*\*103\*\*, 023323 \(2021\)](#).
- [52] X. Wei, X. Gao, and W. Zhu, Static and dynamical Stark many-body localization transition in a linear potential, [Phys. Rev. B \*\*106\*\*, 134207 \(2022\)](#).
- [53] V. D. Naik, F. B. Trigueros, and M. Heyl, Quantum hard disks on a lattice, [arXiv:2311.16240](#).
- [54] M. Will, R. Moessner, and F. Pollmann, Realization of Hilbert Space Fragmentation and Fracton Dynamics in 2D, [arXiv:2311.05695](#).

# Supplementary Materials: Exploring Hilbert-Space Fragmentation on a Superconducting Processor

Yong-Yi Wang,<sup>1,2,\*</sup> Yun-Hao Shi,<sup>1,2,3,\*</sup> Zheng-Hang Sun,<sup>1,4,\*</sup> Chi-Tong Chen,<sup>1,2</sup> Zheng-An Wang,<sup>3,5</sup> Kui Zhao,<sup>3</sup>  
Hao-Tian Liu,<sup>1,2</sup> Wei-Guo Ma,<sup>1,2</sup> Ziting Wang,<sup>3</sup> Hao Li,<sup>3</sup> Jia-Chi Zhang,<sup>1,2</sup> Yu Liu,<sup>1,2</sup> Cheng-Lin Deng,<sup>1,2</sup>  
Tian-Ming Li,<sup>1,2</sup> Yang He,<sup>1,2</sup> Zheng-He Liu,<sup>1,2</sup> Zhen-Yu Peng,<sup>1,2</sup> Xiaohui Song,<sup>1,2</sup> Guangming Xue,<sup>3</sup> Haifeng Yu,<sup>3</sup>  
Kaixuan Huang,<sup>1,3,†</sup> Zhongcheng Xiang,<sup>1,2,‡</sup> Dongning Zheng,<sup>1,2,6,7</sup> Kai Xu,<sup>1,2,3,6,7,§</sup> and Heng Fan<sup>1,2,3,6,7,¶</sup>

<sup>1</sup>*Institute of Physics, Chinese Academy of Sciences, Beijing 100190, China*

<sup>2</sup>*School of Physical Sciences, University of Chinese Academy of Sciences, Beijing 100049, China*

<sup>3</sup>*Beijing Academy of Quantum Information Sciences, Beijing 100193, China*

<sup>4</sup>*Theoretical Physics III, Center for Electronic Correlations and Magnetism,  
Institute of Physics, University of Augsburg, D-86135 Augsburg, Germany*

<sup>5</sup>*Hefei National Laboratory, Hefei 230088, China*

<sup>6</sup>*Songshan Lake Materials Laboratory, Dongguan, Guangdong 523808, China*

<sup>7</sup>*CAS Center for Excellence in Topological Quantum Computation, UCAS,  
Beijing 100190, China, and Mozi Laboratory, Zhengzhou 450001, China*

## CONTENTS

Frequency Arrangement	3
Multi-Qubit Calibration	3
Z Crosstalk Correction	3
Timing Calibration	4
On-Site Potential	4
Model and Hamiltonian	5
Jordan-Wigner Transformation for the $XX$ -Ladder Model	5
Level Statistics	6
Participation entropy for Gaussian orthogonal ensemble and Gaussian unitary ensemble	7
Derivation	7
Numerical verification	8
Statistical Properties of Eigenstates in Stark Systems	8
Participation entropy	8
Entanglement entropy	10
Domain wall number	10
Numerical Krylov Subspace	11
Time Evolution with Krylov Space Method	12
Post-Selection of Measurement Results	13
References	13



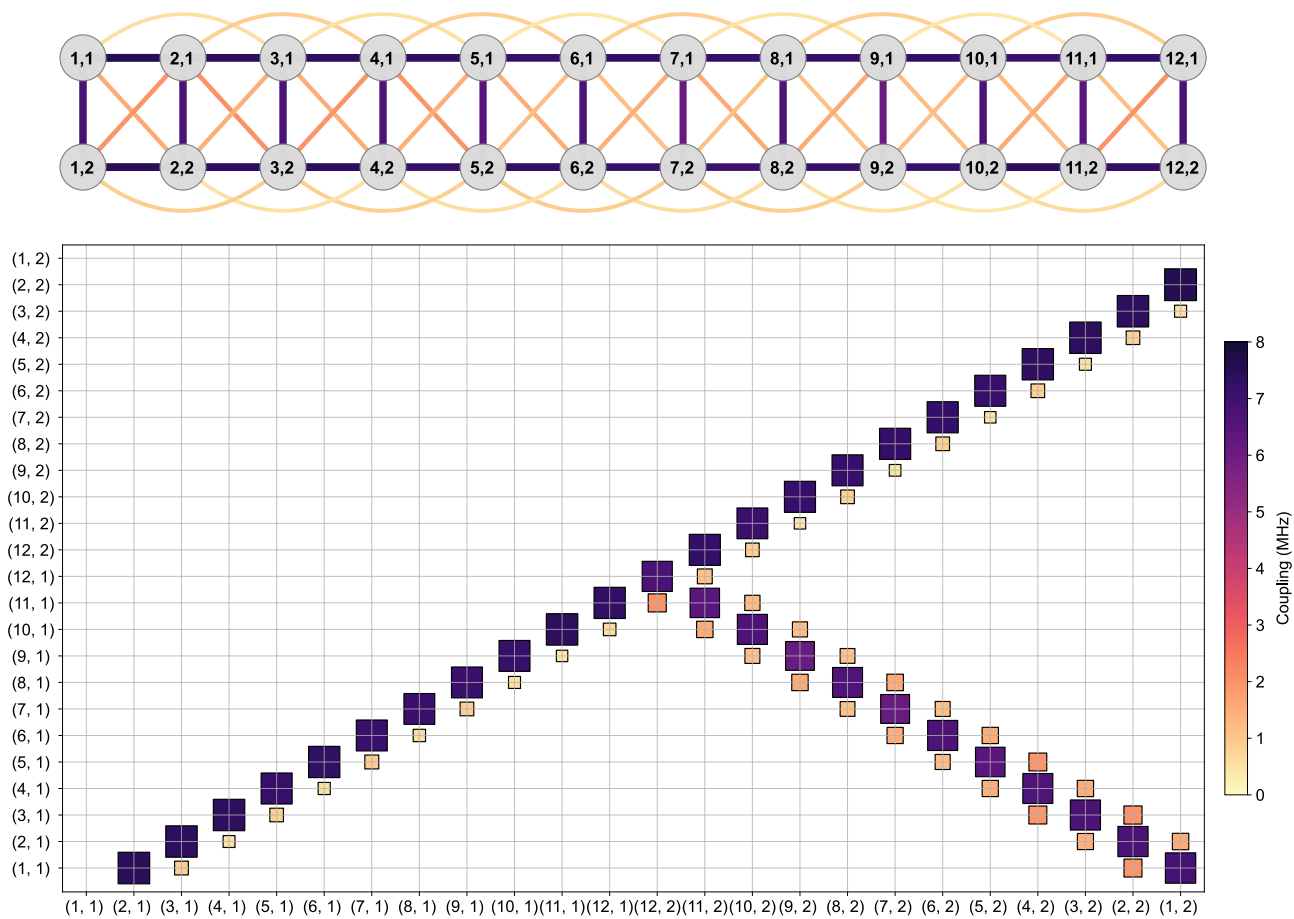


FIG. S1. Coupling strengths of the 24 qubits used in the ladder-type chip.

## FREQUENCY ARRANGEMENT

Before multi-qubit experiments, we also need to arrange the idle frequency of each single qubit to ensure a long coherence time and a low level of XY crosstalk. We optimize the frequency arrangement by considering the two-level system (TLS), the overlap of energy levels, and the residual coupling between qubits.

- To avoid TLS, we can measure the energy relaxation time  $T_1$  near the idle point. If the TLS is coupled to the qubit near the idle point, then the curve of  $T_1$  will drop sharply or oscillate. Besides, the dephasing time  $T_2$  also needs to be considered.
- If the qubit at the idle point has the transition frequency of  $\omega_{10}$  from  $|0\rangle$  to  $|1\rangle$  and the transition frequency of  $\omega_{21}$  from  $|1\rangle$  to  $|2\rangle$ , we should avoid overlapping  $\omega_{10}$ ,  $\omega_{21}$ , and the two-photons frequency  $(\omega_{10} + \omega_{21})/2$ . In addition, the leakage frequencies when we excite the qubit cannot overlap with these frequencies. Specifically, the leakage frequencies include  $\omega_c$  (intrinsic leakage) and  $2\omega_c - \omega_{10}$  (mirror leakage), where  $\omega_c$  denotes the carrier frequency.
- The XY crosstalk includes classical microwave crosstalk and quantum crosstalk. The classical microwave crosstalk can be effectively suppressed by appropriately increasing the duration of the excitation microwave pulse (reducing the broadening in the frequency domain). In our experiment, we set the duration of  $\pi$  pulse to 120 ns. However, the quantum crosstalk resulting from the residual coupling between qubits can only be reduced by changing the frequencies and increasing the qubit frequency difference.

Parameter	Median	Mean	Stdev.	Units
Qubit maximum frequency	5.025	5.032	0.240	GHz
Qubit idle frequency	4.723	4.728	0.346	GHz
Qubit anharmonicity	-0.222	-0.222	0.022	GHz
Readout frequency	6.715	6.714	0.061	GHz
Mean energy relaxation time $\bar{T}_1$	33.2	32.1	7.5	$\mu$ s
Pure dephasing time at idle frequency $T_2^*$	1.0	2.4	4.2	$\mu$ s

TABLE S1. List of device parameters. Reproduced from Ref. [1].

## MULTI-QUBIT CALIBRATION

After single-qubit calibration, we implement multi-qubit calibration to correct the crosstalk, align the timing, and find the control parameters of qubits to achieve the target Hamiltonian with high precision. The reference frequency is fixed at 4.534 GHz, and the on-site potential manipulated in the experiment is the difference between the qubit frequency and this reference frequency.

## Z Crosstalk Correction

The Z crosstalk results from the fact that the low-frequency Z bias signal is not completely localized to a single qubit. The individual Z bias signal of each qubit has a spatial distribution across the chip, but the strength decays with the distance between qubits. Assuming that the Z pulse amplitude (Zpa) of the  $j$ -th qubit  $Q_j$  is  $z_j$ , and the vertical distance between its Z control line and the  $i$ -th qubit  $Q_i$  is  $r_{i,j}$ , then the magnetic induction strength felt by  $Q_i$  from the Z line of the  $Q_j$  can be expressed as  $B_{i\leftarrow j} \propto z_j/r_{i,j}$ . The corresponding crosstalk flux thus is  $\Phi_{i\leftarrow j} = B_{i\leftarrow j}S_i = c_{i\leftarrow j}z_j$ , where  $S_i$  represents the loop area of  $Q_i$ 's SQUID and  $c_{i\leftarrow j} \propto S_i/r_{i,j}$  denotes the flux crosstalk per unit Zpa. To compensate for the crosstalk  $\Phi_{i\leftarrow j}$ , we apply  $\Phi_{i\leftarrow i} = c_{i\leftarrow i}z_i$  on the Z line of  $Q_i$  to satisfy

$$\Phi_{i\leftarrow i} = -\Phi_{i\leftarrow j}, \quad (\text{S1})$$

thus the Z crosstalk coefficient of  $Q_j$  to  $Q_i$  can be calculated as

$$M_{i,j} = \frac{c_{i\leftarrow j}}{c_{i\leftarrow i}} = -\frac{z_i}{z_j}. \quad (\text{S2})$$

For each  $z_j$ , we scan the Zpa of  $Q_i$  to find the corresponding  $z_i$  for compensation. Hence, the Z crosstalk coefficient  $M_{i,j}$  can be determined by linear fitting. As shown in Fig. S2(a), we apply an XY drive pulse to the target qubit  $Q_i$  while scanning its Zpa to compensate for the crosstalk from the Zpa of the source  $Q_j$ . If the crosstalk is compensated exactly, then we will measure a high probability of  $Q_i$  in  $|1\rangle$ . Typical experimental data are shown in Fig. S2(c) and S2(d). Note that the

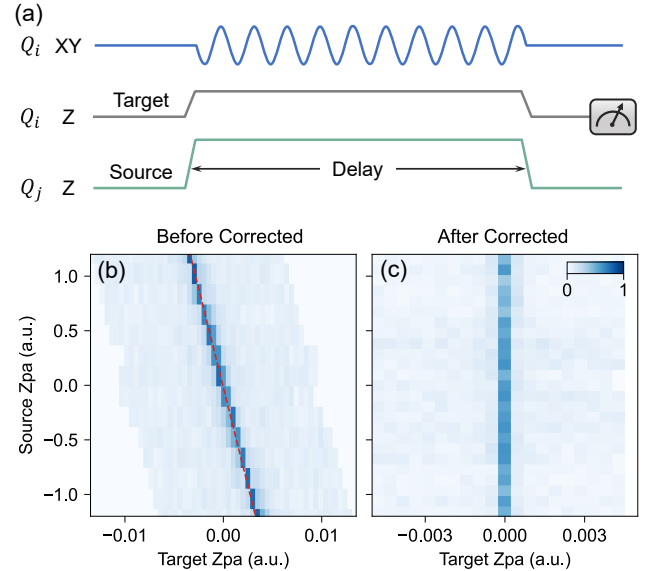


FIG. S2. Typical experimental data of measuring Z crosstalk. (a) Pulse sequences for measuring the Z crosstalk coefficient of  $Q_j$  to  $Q_i$ , i.e.,  $M_{i,j}$ . Here we fix the delay at  $1.5 \mu$ s to suppress the broadening of data. (b) Heatmap showing the probability of  $Q_i$  in  $|1\rangle$  before and after the Z crosstalk correction. The red dash line is the result of linear fitting to obtain  $M_{i,j}$ .

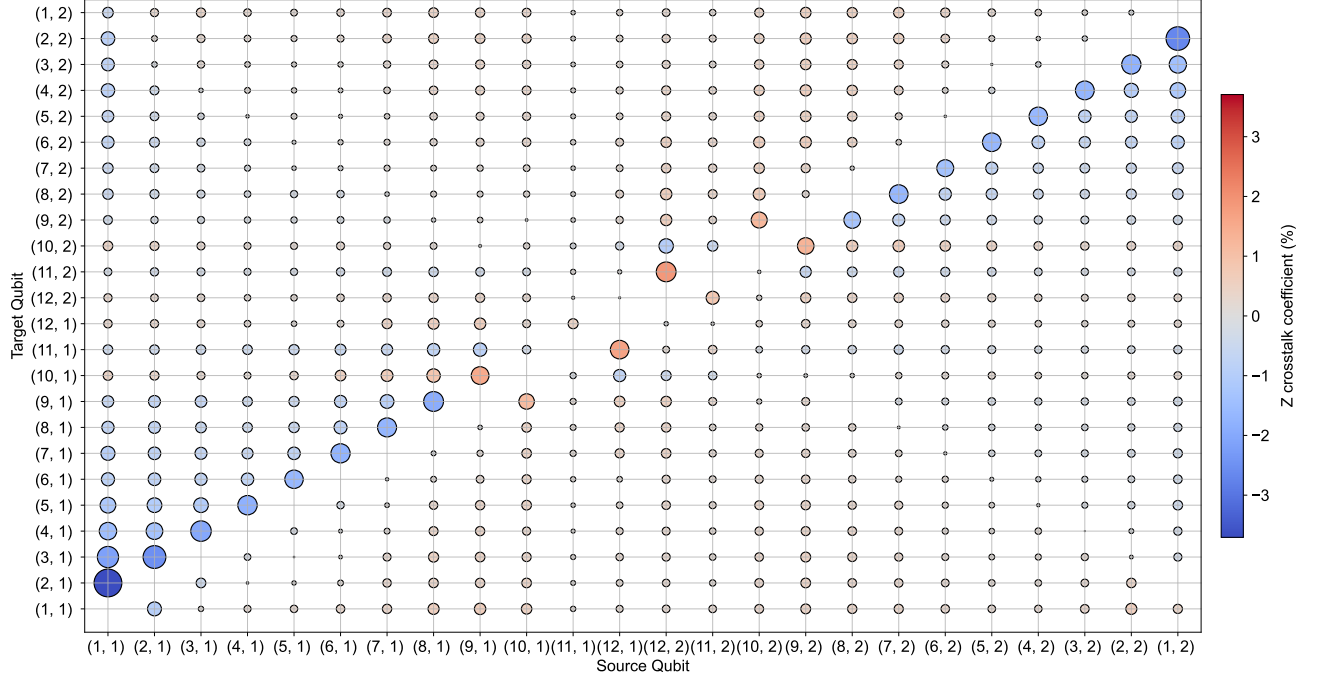


FIG. S3. **Off-diagonal Z crosstalk matrix.** The heatmap shows the Z crosstalk coefficient  $M_{i,j}$  ( $i \neq j$ ). The size of the colored bubble represents  $|M_{i,j}|$ . Here we show the crosstalk coefficients of the 24 qubits used in the ladder-type chip.

above Z crosstalk is linear and does not take into account the anti-cross effect of energy levels when qubits are close to each other. When measuring such linear crosstalk, it is preferable to adjust the step of the scanned source Zpa so that the frequency change corresponding to each scanning step is greater than twice the coupling strength. Thus, the impact of the anti-cross effect on the measured data will be reduced.

After measuring the Z crosstalk coefficient for each pair of qubits, we obtain the whole crosstalk matrix  $\mathbf{M}$  (Fig. S3). In the subsequent multi-qubit calibration and experiments, we will implement the following correction to the Z pulses of all the qubits:

$$\mathbf{z}_{\text{corrected}} = \mathbf{M}^{-1}\mathbf{z}, \quad (\text{S3})$$

where  $\mathbf{M}^{-1}$  is the inverse of  $\mathbf{M}$ ,  $\mathbf{z} = [z_1, z_2, \dots]^T$  denotes the vector of all the Zpas, and  $\mathbf{z}_{\text{corrected}}$  represents the corrected vector.

### Timing Calibration

In single-qubit timing calibration, we have calibrated the timing between each qubit's own XY and Z signals. However, different qubits have different control line lengths and this causes a timing shift between qubits. Here we introduce an efficient method to automatically calibrate the timing between qubits (Fig. S4):

- Find the Zpa corresponding to the two-qubit resonance: We initially prepare  $|10\rangle$  by applying a  $\pi$  pulse to  $Q_i$ ,

then vary the Zpa of  $Q_j$  (the Zpa of  $Q_i$  is fixed near the resonance point) and measure the joint probabilities  $P_{|01\rangle}$  and  $P_{|10\rangle}$ , see Fig. S4(b). For these probabilities to change significantly as the Zpa of  $Q_j$  approaches the resonance point, we choose the delay to be approximately half of the swap period, i.e.,  $t_d \approx T/2$ , where  $T = \pi/g$  is the swap period and  $g$  denotes the coupling strength of qubits. Here the coupling strength only needs to be given a rough value and does not need to be finely measured.

- Determine a sensitive delay time of the swap: With the Zpa of  $Q_j$  corresponding to the resonance, we measure  $P_{|01\rangle}$  and  $P_{|10\rangle}$  as the function of delay, see Fig. S4(c). By fitting this data with the cosine function, we can obtain the exact swap period  $T$ . The sensitive delay time is near where the derivative is at its maximum ( $\approx T/4$ ). Here we choose a delay slightly less than  $T/4$  for the next step.
- Optimize the relative time shift between two qubits: We measure  $P_{|01\rangle}$  and  $P_{|10\rangle}$  as the function of  $Q_j$ 's time shift and fit them with Gaussian functions, see Fig. S4(d). The optimal time shift is at the peak (or dip) of the Gaussian function.

### On-Site Potential

Our experiment requires a high-precision control of on-site disorder and Stark potential. Even though we have

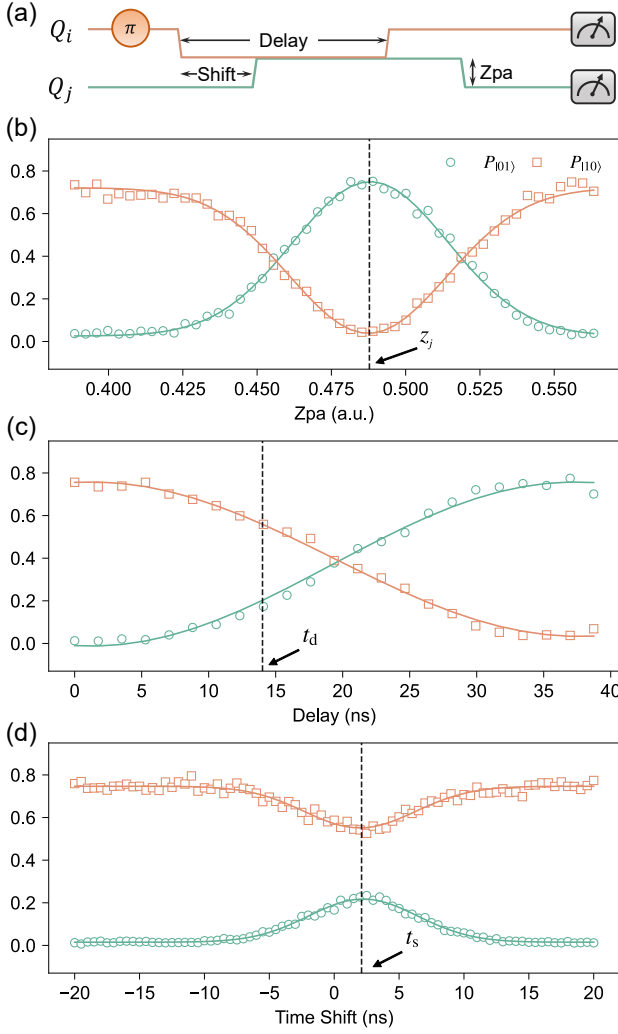


FIG. S4. **Typical experimental data of timing calibration.** (a) Pulse sequences of two-qubit swap experiment for timing calibration. (b) Joint probabilities  $P_{|01\rangle}$  and  $P_{|10\rangle}$  as the function of the Zpa of  $Q_j$ . By fitting this data with the cosine function, we obtain the swap period  $T$ . Then we determine the delay  $t_d$  slightly less than  $T/4$ . (c) Joint probabilities as the function of delay. (d) Joint probabilities as the function of time shift. The optimal time shift  $t_s$  applied to  $Q_j$  is calculated as the average of the Gaussian fitting results.

corrected the linear Z crosstalk and aligned the timing, the qubit (dressed-)frequency will still deviate from the target frequency when other qubits are simultaneously biased. This effect mainly comes from the interaction with other qubits (if the residual Z crosstalk is relatively negligible). Here we introduce a method to suppress this effect and calibrate qubit frequencies with a high precision.

As shown in Fig. S5, there are two configurations for the calibration, namely A and B. Configuration A requires that the nearest-neighbor (NN) qubits, the next-nearest-neighbor (NNN) qubits, and the rest qubits biased from the target frequency of  $+\Delta_{\text{NN}}$ ,  $+\Delta_{\text{NNN}}$ , and  $+\Delta_{\text{rest}}$ , respectively. Thus, the dressed frequency of the target qubit  $Q_i$  can be approximately

expressed as

$$\tilde{\omega}_i^{\text{A}} \approx \omega_i + \sum_{j \neq i} \frac{g_{i,j}^2}{\Delta_j}, \quad (\text{S4})$$

where  $\omega_i$  denotes the target frequency,  $g_{i,j}$  is the coupling strength, and  $\Delta_j = \omega_i - \omega_j$  is the frequency detuning. Similarly, for configuration B with the opposite detuning, we have

$$\tilde{\omega}_i^{\text{B}} \approx \omega_i - \sum_{j \neq i} \frac{g_{i,j}^2}{\Delta_j}. \quad (\text{S5})$$

We perform the Rabi oscillation experiments under these two configurations, and thus determine the corresponding Zpas of  $\tilde{\omega}_i^{\text{A}}$  and  $\tilde{\omega}_i^{\text{B}}$ , i.e.,  $z_i^{\text{A}}$  and  $z_i^{\text{B}}$  (Fig. S6).

To ensure a large adjustment range of Zpa, we usually set the target frequency below the maximum frequency of the qubit with the smallest maximum frequency. The relationship between the qubit's Zpa and frequency near such target frequencies is monotonic. Hence, the corresponding Zpa of the target  $\omega_i$  can be approximately calculated as the average of  $z_i^{\text{A}}$  and  $z_i^{\text{B}}$ :

$$z_i = f(\omega_i) \approx \frac{1}{2} [f(\tilde{\omega}_i^{\text{A}}) + f(\tilde{\omega}_i^{\text{B}})] = \frac{1}{2} (z_i^{\text{A}} + z_i^{\text{B}}), \quad (\text{S6})$$

where  $f$  is a monotonic function that represents the relationship between qubit's Zpa and frequency near the target frequency. For each qubit, we repeat the above calibration procedure and finally obtain the Zpas of all qubits corresponding to the target on-site potentials. The schematic of experimental pulse sequences is shown in Fig. S7.

## MODEL AND HAMILTONIAN

### Jordan-Wigner Transformation for the $XX$ -Ladder Model

The main interacting term of the Hamiltonian describing our superconducting processor can be approximated as the  $XX$ -ladder model. The approximating ladder- $XX$  model can be mapped to an interacting spinless fermion model, utilizing a generalized form of Jordan-Wigner transformation, described as

$$\hat{S}_{j,1}^- = \hat{c}_{j,1} \exp \left[ i\pi \sum_{l=0}^{j-1} (\hat{n}_{l,1} + \hat{n}_{l,2}) \right], \quad (\text{S7})$$

for the first row of chain, and

$$\hat{S}_{j,2}^- = \hat{c}_{j,2} \exp \left[ i\pi \left[ \sum_{l=0}^j \hat{n}_{l,1} + \sum_{l=0}^{j-1} \hat{n}_{l,2} \right] \right], \quad (\text{S8})$$

for the second row of chain, where  $\hat{S}_{j,m}^- = (\hat{\sigma}_{j,m}^x - i\hat{\sigma}_{j,m}^y)/2$  ( $j = 1, 2, \dots, L$  and  $m = 1, 2$ ) and  $\hat{n}_{j,m} = \hat{c}_{j,m}^\dagger \hat{c}_{j,m}$  is the spinless fermion number operator for site  $(j, m)$ . Therefore,



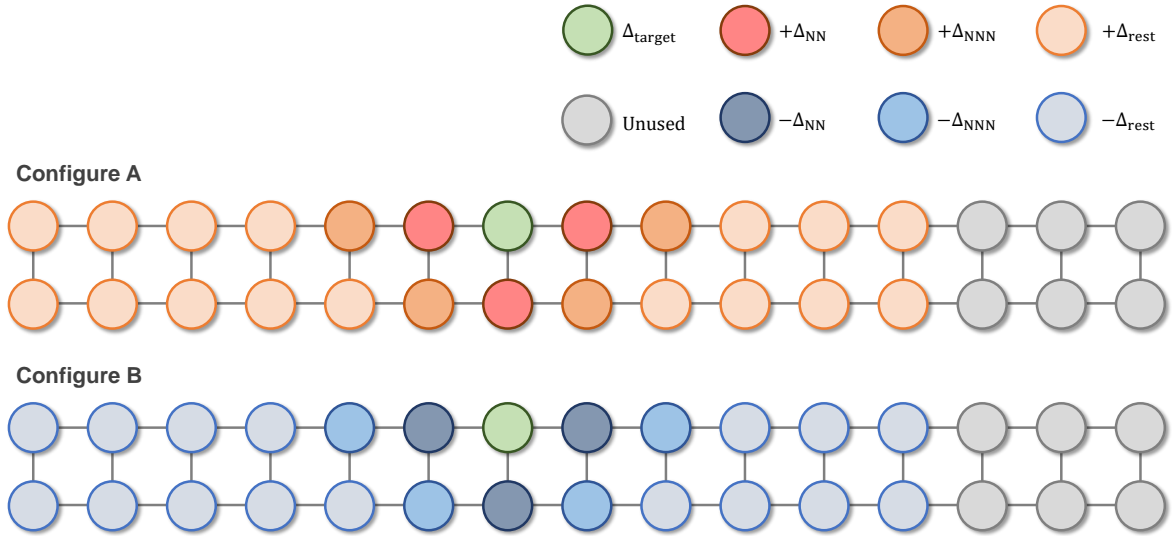


FIG. S5. **Configurations for multi-qubit calibration.** As an example, here we take  $Q_{7,\uparrow}$  as the target qubit. The frequency differences are  $\Delta_{\text{NN}}/2\pi \approx 160$  MHz,  $\Delta_{\text{NNN}}/2\pi \approx 50$  MHz and  $\Delta_{\text{rest}}/2\pi \approx 25$  MHz. All unused qubits ( $Q_{13,\uparrow}$ ,  $Q_{13,\downarrow}$ ,  $Q_{14,\uparrow}$ ,  $Q_{14,\downarrow}$ ,  $Q_{15,\uparrow}$ ,  $Q_{15,\downarrow}$ ) are biased away from the reference frequency.

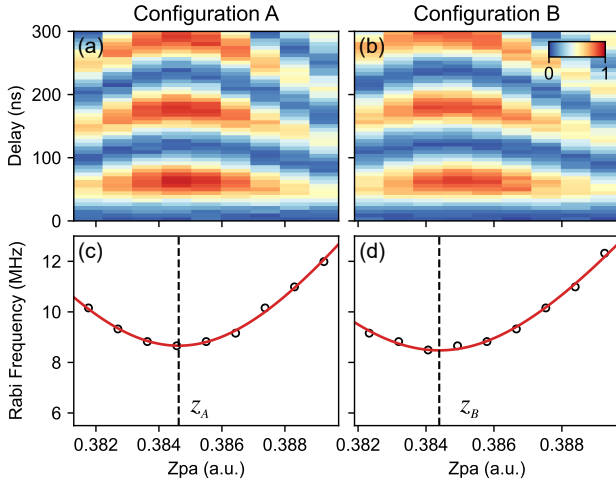


FIG. S6. **Typical experimental data of calibrating on-site potential.** The results of Rabi oscillation experiments under configurations A (a) and B (b). The heatmap shows the probability of the target qubit in  $|1\rangle$ . (c) and (d) correspond to (a) and (b), respectively, representing the Rabi frequency as a function of  $Z_{\text{pa}}$ .

the Hamiltonian in the spinless fermion representation reads

$$\begin{aligned} \hat{H} = & -2J \sum_{j,\delta} [\hat{c}_{j,1} \exp(-i\pi\hat{\phi}_{j,j+\delta}^{(1)}) \hat{c}_{j+\delta,1}^\dagger \\ & + \hat{c}_{j,1} \exp(-i\pi\hat{\phi}_{j,j+\delta}^{(2)}) \hat{c}_{j+\delta,2}^\dagger] \\ & - 2J \sum_j \hat{c}_{j,1} \hat{c}_{j,2}^\dagger, \end{aligned} \quad (\text{S9})$$

where  $\delta$  denotes the nearest neighbor, and  $\hat{\phi}_{j,j+1}^{(1)} = \hat{n}_{j,2}$ ,  $\hat{\phi}_{j,j-1}^{(1)} = -\hat{n}_{j-1,2}$ ,  $\hat{\phi}_{j,j+1}^{(2)} = \hat{n}_{j,1}$ ,  $\hat{\phi}_{j,j-1}^{(2)} = -\hat{n}_{j-1,1}$ . The

many-body interaction in the Hamiltonian leads to the nonintegrability and many-body quantum chaos.

### Level Statistics

In this work, we study systems in both Stark potentials  $W_{jm}/\bar{J}_{\text{NN}} = -j\gamma$ , and random potentials  $W_{jm}/\bar{J}_{\text{NN}}$  drawn from a uniform distribution in  $[-W, W]$ , as illustrated in the upper and lower panel of Fig. S8(a), respectively. With the increasing of the gradient  $\gamma$  or the disorder strength  $W$ , a transition from ergodicity to localization is expected in this typical nonintegrable model.

A common numerical way to characterize the ergodicity and MBL is the level statistics based on random matrix theory, quantified by the ratio of adjacent level spacings  $r^{(n)} = \min(\delta^{(n)}, \delta^{(n+1)}) / \max(\delta^{(n)}, \delta^{(n+1)})$  with  $\delta^{(n)} = E_n - E_{n-1} > 0$ . As the gradient  $\gamma$  (or the disorder strength  $W$ ) increases, the level statistics changes from the Wigner-Dyson distribution with the average  $\langle r \rangle \simeq 0.531$  in the ergodic phase, to the Poisson distribution with  $\langle r \rangle \simeq 0.386$  in the many-body localized phase (see Fig. S8(b)).

It is worth noting that, across all parameters depicted in Fig. 3 and Fig. 4, the average ratio of adjacent level spacings  $\langle r \rangle$  consistently remains close to 0.531, signifying thermalization for at least the majority of spectrum.

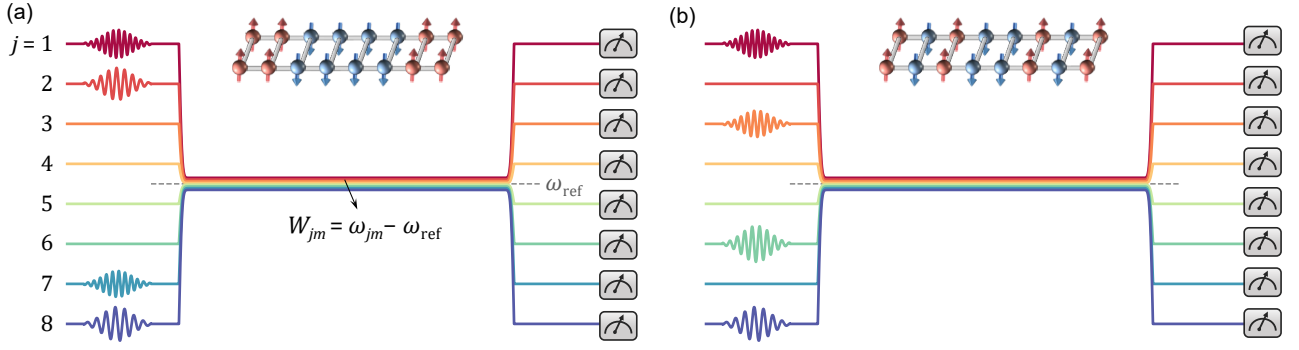


FIG. S7. **Schematic of experimental pulse sequences for different initial states.** Here we take the case of  $L = 8$  as an example, where the initial states  $|\psi_{n_{DW}=2}\rangle = |11000011\rangle$  and  $|\psi_{n_{DW}=6}\rangle = |10100101\rangle$  correspond to (a) and (b), respectively. The on-site potential  $W_{jm}$  is denoted as the difference between the qubit frequency  $\omega_{jm}$  and the reference frequency  $\omega_{\text{ref}}$ . By controlling the Zpas of qubits, we manipulate  $\omega_{jm}$  to realize the Stark (linear) potentials  $W_{jm}/J_{\text{NN}} = -j\gamma$ , or random potentials  $W_{jm}/J_{\text{NN}}$  with a uniform distribution in  $[-W, W]$ .

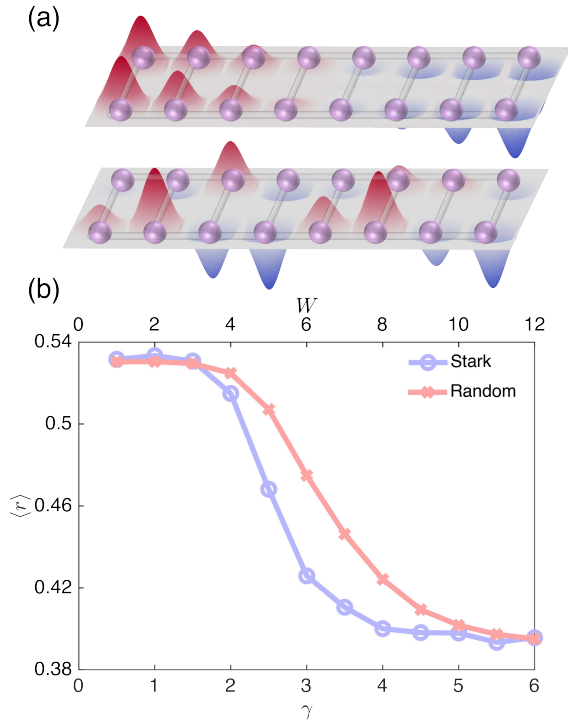


FIG. S8. **Ergodicity to localization transition in Stark and random potentials.** (a) Schematic representation of the Stark potentials and random potentials sampled from a uniform distribution to study the transition from ergodicity to localization. All qubits are adjusted to corresponding frequencies deviated from the center frequency  $\approx 4.534$  GHz. (b) The ratio of adjacent level spacings as the function of gradient  $\gamma$  or the disorder strength  $W$ , with level statistics from the ergodic Wigner-Dyson distribution ( $\langle r \rangle \approx 0.531$ ) to the many-body localized Poisson distribution ( $\langle r \rangle \approx 0.386$ ).

### Participation entropy for Gaussian orthogonal ensemble and Gaussian unitary ensemble

#### Derivation

Here, we give a direct derivation of the participation entropy predicted by the Gaussian orthogonal ensemble (GOE) and the Gaussian unitary ensemble (GUE), which corresponds to the eigenstates and the generic long-time-evolved states, respectively, for a typical nonintegrable model [2, 3].

For the GOE, the  $N$  components of an eigenvector is real number, and its norm must be one. Therefore,

$$P_{\text{GOE}}(\mathbf{c}) = C_N \delta\left(1 - \sum_{n=1}^N c_n^2\right). \quad (\text{S10})$$

For the function of random variants  $f(\mathbf{x})$  subjects to distribution  $P(f)$ , we have  $P(f) = \int d\mathbf{x} \delta(P - f(\mathbf{x})) p(\mathbf{x})$ . So the marginal distribution of a single component by

$$P_{\text{GOE}}(p) = \int dc_1 \cdots dc_N \delta(p - c_i^2) P_{\text{GOE}}(\mathbf{c}). \quad (\text{S11})$$

Defining

$$P_{\text{GOE}}(p; t) = \int dc_1 \cdots dc_N \delta(p - c_i^2) C_N \delta\left(t - \sum_{n=1}^N c_n^2\right), \quad (\text{S12})$$

and taking the Laplace transform, we have:

$$\begin{aligned} & \int_0^\infty dt e^{-st} P_{\text{GOE}}(p; t) \\ &= C_N \int dc_i \delta(p - c_i^2) e^{-sc_i^2} \left( \int dc e^{-sc^2} \right)^{N-1} \\ &\propto \frac{e^{-sp}}{\sqrt{p} s^{(N-1)/2}}. \end{aligned} \quad (\text{S13})$$

Then inverting the Laplace transform, we finally get

$$\begin{aligned} P_{\text{GOE}}(p; t) &\propto (t-p)^{(N-3)/2} \theta(t-p) / \sqrt{p} \\ \Rightarrow P_{\text{GOE}}(p) = P_{\text{GOE}}(p; 1) &= \frac{1}{\sqrt{\pi}} \frac{\Gamma(N/2)}{\Gamma((N-1)/2)} \frac{(1-p)^{(N-3)/2}}{\sqrt{p}}. \end{aligned} \quad (\text{S14})$$

Therefore,  $P_{\text{GOE}}(p) \propto \exp(-Np/2) / \sqrt{p}$  for large  $N \gg 1$ , and

$$\begin{aligned} S_{\text{GOE}}^{\text{PE}} &= - \sum_i^N p_i \log p_i \\ &= -N \int_0^\infty P_{\text{GOE}}(p) p \log(p) dp \\ &\propto -N \int_0^\infty \exp(-Np/2) \sqrt{p} \log(p) dp. \end{aligned} \quad (\text{S15})$$

Finally, we get  $S_{\text{GOE}}^{\text{PE}} = \log N - 2 + \log(2) + \gamma_e \approx \log 0.482N$ , with  $\gamma_e$  being Euler's constant.

Similarly, since the only constraint on  $N$  components of an eigenvector for the GUE is that its norm be one, we have

$$P_{\text{GUE}}(\mathbf{c}) = C_N \delta \left( 1 - \sum_{n=1}^N |c_n|^2 \right). \quad (\text{S16})$$

Defining

$$P_{\text{GUE}}(p; t) = \int d^2 c_1 \cdots d^2 c_N \delta(p - |c_i|^2) C_N \delta \left( t - \sum_{n=1}^N |c_n|^2 \right), \quad (\text{S17})$$

and taking the Laplace transform:

$$\begin{aligned} &\int_0^\infty dt e^{-st} P_{\text{GUE}}(p; t) \\ &= C_N \int d^2 c_i \delta(p - |c_i|^2) e^{-s|c_i|^2} \left( \int d^2 c e^{-s|c|^2} \right)^{N-1} \\ &\propto \frac{e^{-sp}}{s^{N-1}}, \end{aligned} \quad (\text{S18})$$

then inverting the Laplace transform, we finally get

$$\begin{aligned} P_{\text{GUE}}(p; t) &\propto (t-p)^{N-2} \theta(t-p) \\ \Rightarrow P_{\text{GUE}}(p) = P_{\text{GUE}}(p; 1) &= (N-1)(1-p)^{N-2}. \end{aligned} \quad (\text{S19})$$

Therefore,  $P_{\text{GUE}}(p) = N \exp(-Np)$  for large  $N \gg 1$ , and

$$\begin{aligned} S_{\text{GUE}}^{\text{PE}} &= - \sum_i^N p_i \log p_i \\ &= -N \int_0^\infty p N e^{-Np} \log p dp \\ &= \log N - 1 + \gamma_e \end{aligned} \quad (\text{S20})$$

*Numerical verification*

As stated before, the Hamiltonian [Eq. (1)] in the main text without the on-site potential is a typical nonintegrable model,

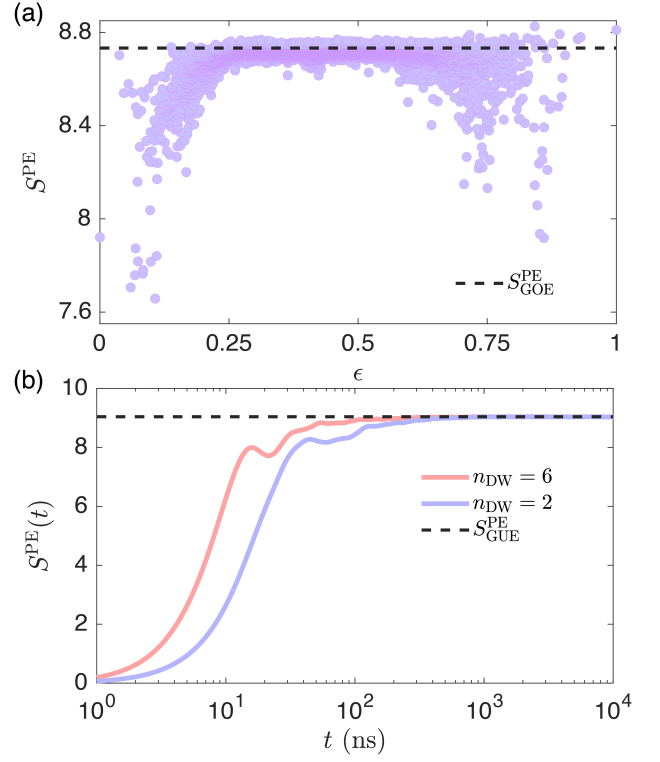


**FIG. S9. Participation entropy for the  $XX$ -ladder model.** (a) Participation entropy of the eigenstate against its normalized energy. The dashed line represent  $S_{\text{GOE}}^{\text{PE}} \approx 8.73$ . (b) Time-evolution of participation entropy for the initial states  $|\psi_{n_{\text{DW}}=6}\rangle = |\mathbb{10100101}\rangle$  and  $|\psi_{n_{\text{DW}}=2}\rangle = |\mathbb{11000011}\rangle$ . The dashed line represent  $S_{\text{GUE}}^{\text{PE}} \approx 9.04$ .

for which the PE of highly excited eigenstates will be close to  $S_{\text{GOE}}^{\text{PE}} = \log \mathcal{N} - 2 + \log(2) + \gamma_e$ . At the same time, the time-evolved states for generic initial states correspond to eigenvectors of a random matrix in the GUE, of which the PE will be  $S_{\text{GUE}}^{\text{PE}} = \log \mathcal{N} - 1 + \gamma_e$ .

Here, we numerically calculate the PE of all eigenstates for the  $XX$ -ladder model with the system size  $8 \times 2$ . The PE is plotted against the normalized energy  $\epsilon = \frac{E - E_{\min}}{E_{\max} - E_{\min}}$  for each eigenstate in Fig. S9(a). The PE of highly excited eigenstates ( $\epsilon \approx 0.5$ ) is very close to  $S_{\text{GOE}}^{\text{PE}} \approx 8.73$ . We also plot the time-evolution of PE for initial states  $|\psi_0\rangle = |\psi_{n_{\text{DW}}=6}\rangle$  and  $|\psi_{n_{\text{DW}}=2}\rangle$  in Fig. S9(b). We can see that in a few hundred nanoseconds, the PE closely approximates  $S_{\text{GUE}}^{\text{PE}} \approx 9.04$  for both initial states.

## Statistical Properties of Eigenstates in Stark Systems

### Participation entropy

To quantify the localization in Hilbert space of spin configurations, we can calculate the PE of all eigenstates with exact

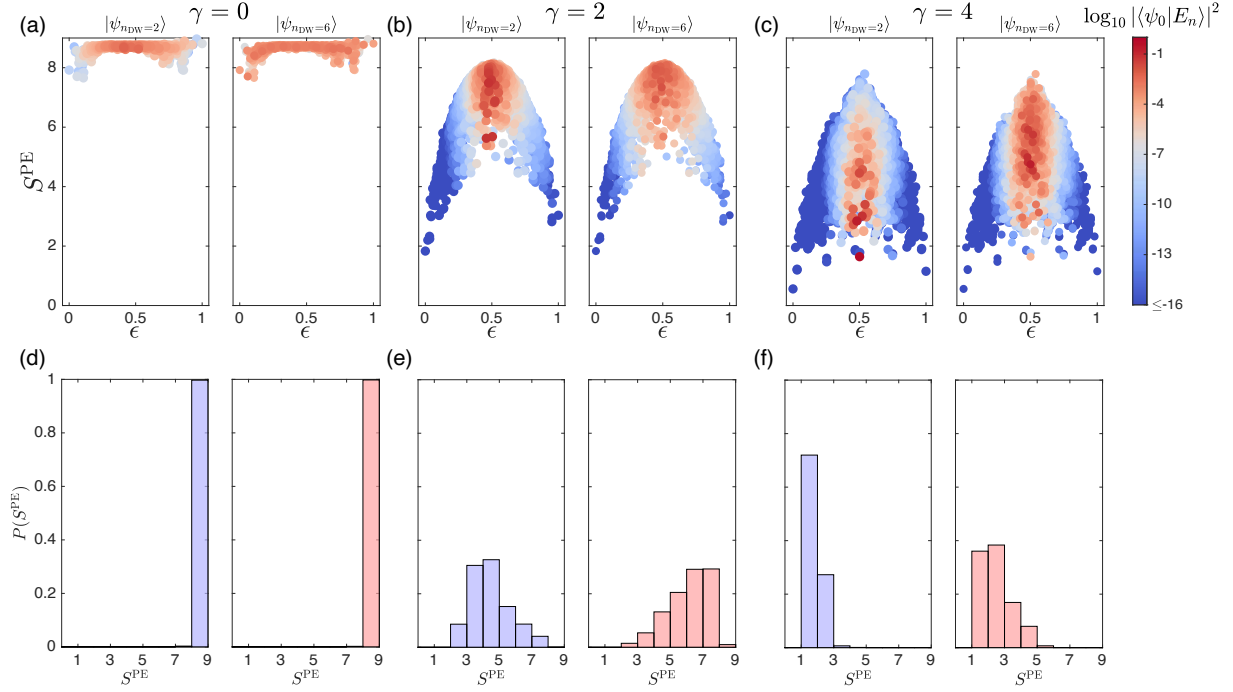


FIG. S10. **Participation entropy of Eigenstates in Stark Systems.** (a–c) Participation entropy of eigenstates for a Stark potential with the gradient  $\gamma = 0, 2$  and  $4$ . The colorbar indicates the logarithm of the eigenstate occupation numbers  $\log_{10} |\langle \psi_0 | E_n \rangle|^2$  for the initial states  $|\psi_{n_{\text{DW}}=2}\rangle$  and  $|\psi_{n_{\text{DW}}=6}\rangle$ . (d–f) Histogram of the participation entropy at  $\gamma = 0, 2$  and  $4$  in the diagonal ensembles corresponding to the initial states  $|\psi_{n_{\text{DW}}=2}\rangle$  and  $|\psi_{n_{\text{DW}}=6}\rangle$ .

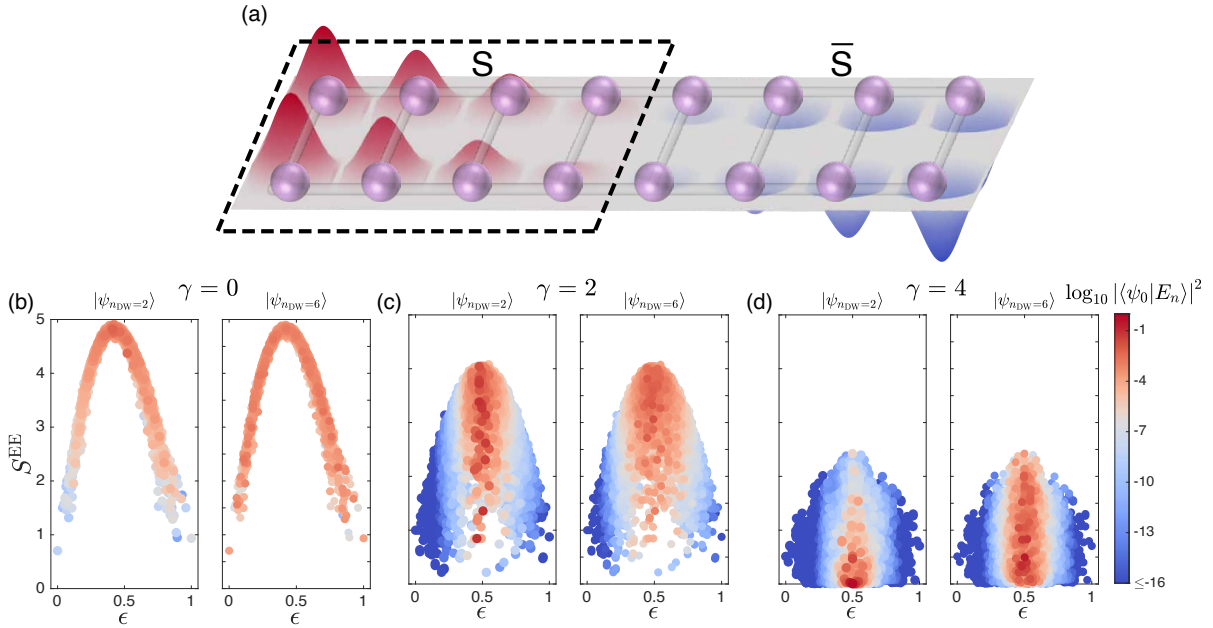


FIG. S11. **Entanglement entropy of eigenstates in Stark Systems.** (a) Half-chain entanglement cut (region S) of the ladder. (b–d) Entanglement entropy of eigenstates for a Stark potential with the gradient  $\gamma = 0, 2$  and  $4$ . The colorbar indicates the logarithm of the eigenstate occupation numbers  $\log_{10} |\langle \psi_0 | E_n \rangle|^2$  for the initial states  $|\psi_{n_{\text{DW}}=2}\rangle$  and  $|\psi_{n_{\text{DW}}=6}\rangle$ .



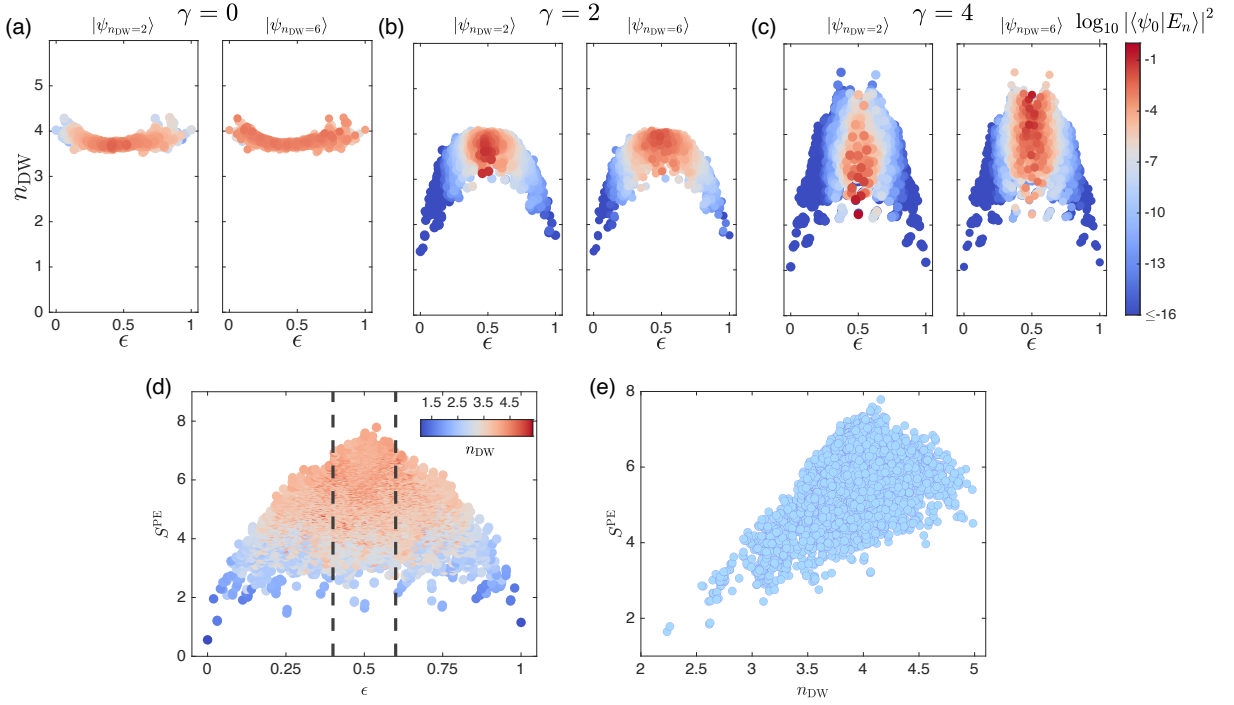


FIG. S12. **Domain wall number of eigenstates in Stark Systems.** (a–c) Domain wall number of eigenstates for a Stark potential with the gradient  $\gamma = 0, 2$  and  $4$ . The colorbar indicates the logarithm of the eigenstate occupation numbers  $\log_{10} |\langle \psi_0 | E_n \rangle|^2$  for the initial states  $|\psi_{n_{\text{DW}}=2}\rangle$  and  $|\psi_{n_{\text{DW}}=6}\rangle$ . (d) Participation entropy of eigenstates at  $\gamma = 4$  with the colorbar representing the domain wall number  $n_{\text{dw}}$ . (e) Participation entropy as a function of  $n_{\text{DW}}$  for eigenstates with  $\epsilon \in [0.4, 0.6]$ , corresponding to the region between the dashed lines in (d).

diagonalization, defined as

$$S^{\text{PE}}(n) = - \sum_i^{\mathcal{N}} p_i(n) \log p_i(n), \quad (\text{S21})$$

where  $p_i(n) = |\langle i | E_n \rangle|^2$ , with  $\{|i\rangle\}$  being spin configuration basis, and  $\mathcal{N}$  is the dimension of Hilbert space ( $\mathcal{N} = \binom{16}{8} = 12870$  for the  $Q = L$  sector with  $L = 8$ ).

In Fig. S10(a–c), the PE of eigenstates is displayed for the Hamiltonian [Eq. (1)] with a Stark potential at  $\gamma = 0, 2$  and  $4$ . The colorbars represent the eigenstate occupation numbers  $|\langle \psi_0 | E_n \rangle|^2$  (i.e., the weights that eigenstates  $|E_n\rangle$  have in the diagonal ensemble corresponding to  $|\psi_0\rangle$ ). At  $\gamma = 0$ , the PE  $S^{\text{PE}} \approx S^{\text{GOE}}$  for eigenstates with  $\epsilon \approx 0.5$  (same as in Fig. S9(a)). As  $\gamma$  increases, we can observe that the PE of eigenstates decreases overall, with the range of fluctuations increasing.

We also displayed the histogram of the PE in the diagonal ensembles for  $|\psi_0\rangle = |\psi_{n_{\text{DW}}=2}\rangle$  and  $|\psi_{n_{\text{DW}}=6}\rangle$  in Fig. S10(d–f). For nonzero  $\gamma$ , the histogram of the PE in the diagonal ensemble for  $|\psi_{n_{\text{DW}}=2}\rangle$  tends to distribute more at lower values of PE, compared to the diagonal ensemble for  $|\psi_{n_{\text{DW}}=6}\rangle$ . From the distribution of the PE in the diagonal ensemble, we can infer that in quench dynamics, the PE at long times also differs for different initial states (as illustrated in Fig. 4 of the main text).

### Entanglement entropy

Another quantity that is often used to characterize MBL is the entanglement entropy (EE) [4, 5], defined as

$$S^{\text{EE}}(n) = -\text{Tr}[\hat{\rho}_S(n) \log \hat{\rho}_S(n)], \quad (\text{S22})$$

where  $\hat{\rho}_S(n) = \text{Tr}_{\bar{S}}[|E_n\rangle\langle E_n|]$  is the reduced density matrix of the subsystem  $S$  (with  $\bar{S}$  being the complement of  $S$ ) for the eigenstate  $|E_n\rangle$ . As shown in Fig. S11(a), the subsystem  $S$  considered here is the left half of the ladder. In Fig. S11(b–d), we display the EE of eigenstates for the Hamiltonian [Eq. (1)] with a Stark potential at  $\gamma = 0, 2$  and  $4$ . The colorbars represent the eigenstate occupation numbers  $|\langle \psi_0 | E_n \rangle|^2$  in the diagonal ensemble. Similar to the PE, the EE of eigenstates decreases overall as  $\gamma$  increases, and substantial fluctuations in the EE are observed across the eigenstates for nonzero  $\gamma$ , indicating violations of ETH. At the same time, compared to  $|\psi_0\rangle = |\psi_{n_{\text{DW}}=6}\rangle$ , eigenstates with lower EE exhibit larger eigenstate occupation numbers in the diagonal ensemble for  $|\psi_{n_{\text{DW}}=2}\rangle$ , which implies that the system also exhibits initial-state dependent dynamics in terms of the EE.

### Domain wall number

Besides the PE and the EE, violations of ETH can also be diagnosed from observables like domain wall number, defined

as

$$n_{\text{DW}} = \sum_{j=1}^{L-1} (1 - \langle \hat{\sigma}_j^z \hat{\sigma}_{j+1}^z \rangle) / 2, \quad (\text{S23})$$

with  $\hat{\sigma}_j^z = (\hat{\sigma}_{j,1}^z + \hat{\sigma}_{j,2}^z) / 2$ . In Fig. S12(a–c), we display the domain wall number of the eigenstates, with colorbars being the logarithm of the eigenstate occupation numbers. At  $\gamma = 0$ , according to the ETH, the domain wall numbers  $n_{\text{DW}}$  for the majority of eigenstates are close to the ETH prediction of  $n_{\text{DW}}^{\text{ETH}} \approx 3.73$  for the ladder model. As  $\gamma$  increases, the  $n_{\text{DW}}$  of eigenstates fluctuates, with a number of eigenstates significantly deviating from the ETH prediction. For nonzero  $\gamma$ , eigenstate occupation numbers predominantly distribute on eigenstates with relatively smaller  $n_{\text{DW}}$  in the diagonal ensemble for  $|\psi_{n_{\text{DW}}=2}\rangle$ , but they mainly distribute on eigenstates with larger  $n_{\text{DW}}$  for  $|\psi_{n_{\text{DW}}=6}\rangle$ .

In Fig. S12(d), we plot the PE of eigenstates at  $\gamma = 4$ , where the colorbar represents  $n_{\text{DW}}$ . It is evident that eigenstates with higher PE tend to correspond to larger values of  $n_{\text{DW}}$ . To elucidate this relationship more clearly, in Fig. S12(e), the PE is plotted against  $n_{\text{DW}}$  for eigenstates in the middle of the spectrum,  $\epsilon \in [0.4, 0.6]$ . This illustrates a discernible positive correlation between the PE and  $n_{\text{DW}}$ .

## NUMERICAL KRYLOV SUBSPACE

To illustrate the construction of the numerical Krylov subspace, we firstly introduce the cumulative distribution function (CDF) for a time-evolved state  $|\psi(t)\rangle$ . The calculation of CDF involves the following steps:

- i) Calculate the probabilities of spin configuration basis  $p_i = |\langle \psi(t) | i \rangle|^2$  (i.e., the moduli squared of the wave function coefficients expressed in spin configuration basis  $\{|i\rangle\}$ );
- ii) Sort the probabilities in non-decreasing order, denoted as  $p_{i'}$ , with  $\{i'\}$  representing the sorted indices;
- iii) Compute the CDF as the sum of the sorted probabilities to the index  $n$ , given by  $\text{CDF}(n) = \sum_{i'=1}^n p_{i'}$ .

The CDF defined here illustrates the bases with the probabilities arranged from low to high, contributing to the state, with the curvature representing the degree of unevenness in the distribution. One can expect the CDF would be a straight line for the state with equal weight on all the bases  $\{|i\rangle\}$ , while if the state is a single configuration, the CDF would be 0 for indices  $n \leq \mathcal{N} - 1$  of the sorted basis, and 1 at index  $n = \mathcal{N}$ .

In Fig. S13(a) and (b), we displays the CDF of the time-evolved states for  $|\psi_0\rangle = |\psi_{n_{\text{DW}}=2}\rangle$  and  $|\psi_{n_{\text{DW}}=6}\rangle$  at  $\gamma = 0$ , and 4. For both initial states, the curve of CDF for the time-evolved states lies slightly beneath that for the state with equal weight on all the bases, nearly coinciding with the curve for a random pure state corresponding to the GUE at  $\gamma = 0$ . At  $\gamma = 4$ , the CDF further curve downward for both initial states.

Notably, for  $|\psi_0\rangle = |\psi_{n_{\text{DW}}=2}\rangle$ , the curve is very close to that of a single configuration state, suggesting that the time-evolved state predominantly exhibits high probabilities on only a limited number of bases.

Based on the CDF, we can define the subset  $\mathcal{K}_\delta(t)$  for an initial state as the complement of the cumulative portion of the basis corresponding to the cumulative probabilities  $\delta$ . This subset satisfies  $\sum_{i \in \mathcal{K}_\delta(t)} |\langle \psi(t) | i \rangle|^2 = 1 - \delta$ , as depicted by the shaded region in Fig. S13(a). Therefore, the numerical Krylov subspace  $\mathcal{K}_\delta$  can be further defined as largest subset satisfying  $\arg \max_{\mathcal{K}_\delta(t), t \leq \tau} \{\dim(\mathcal{K}_\delta(t))\}$  within the evolution time  $\tau$  [6].

Here, we calculate  $\mathcal{K}_\delta$  for  $\delta = 0.01$  and  $\tau = 40\mu\text{s}$ , at  $\gamma = 2$ . The dimension of the numerical Krylov subspace is plotted in Fig. S13(c) for the initial states  $|\psi_{n_{\text{DW}}=2}\rangle$  and  $|\psi_{n_{\text{DW}}=L-2}\rangle$  with  $L = 8$  and 12, with the inset showing the dimension of  $\mathcal{K}_\delta(t)$  from  $t = 0$  to  $40\mu\text{s}$ . We observe that the dimension  $\dim \mathcal{K}_\delta(t)$  quickly saturates for  $|\psi_{n_{\text{DW}}=L-2}\rangle$ , regardless of the system size; while for  $|\psi_{n_{\text{DW}}=2}\rangle$ , the growth of  $\dim(\mathcal{K}_\delta(t))$  slows considerably with increasing system length  $L$ . Correspondingly, the dimension of the numerical Krylov Subspace for  $|\psi_{n_{\text{DW}}=2}\rangle$  decreases much more dramatically with increasing  $L$ , compared to  $|\psi_{n_{\text{DW}}=6}\rangle$ . Thus, the numerical Krylov subspaces  $\mathcal{K}_\delta$  exhibit different scaling behaviors for the two initial states, which leads to the initial-state dependent dynamics of the PE as shown in Fig. 4 in the main text.

We have shown that initial states with different  $n_{\text{DW}}$  belong to different fragments, therefore exhibiting distinct dynamics. However, it is worth noting that the reverse is not necessarily valid: initial states sharing the same  $n_{\text{DW}}$  may also each reside within nearly disconnected fragments. Here, we consider a pair of initial states  $\{|\psi_0\rangle, |\bar{\psi}_0\rangle\}$ , which have the maximum Hamming distance  $L \times 2$  between each other [7], with  $|\bar{\psi}_0\rangle = \prod_{j,m} \hat{\sigma}_{jm}^x |\psi_0\rangle$ . For example,  $\{|\psi_{n_{\text{DW}}=2}\rangle = |11000011\rangle, |\bar{\psi}_{n_{\text{DW}}=2}\rangle = |00111100\rangle\}$  and  $\{|\psi_{n_{\text{DW}}=L-2}\rangle = |101000101\rangle, |\bar{\psi}_{n_{\text{DW}}=L-2}\rangle = |01011010\rangle\}$  for  $L = 8$ . From symmetry considerations, one can expect that the initial states  $\{|\psi_0\rangle, |\bar{\psi}_0\rangle\}$  exhibit the same dynamics in terms of PE, EE, imbalance and other quantities. However, this does not necessarily mean these initial states belong to the same fragment. To explore this aspect, we introduce the following quantity:

$$\eta \equiv \frac{\dim(\mathcal{K}_\delta(\psi_0) \cap \mathcal{K}_\delta(\bar{\psi}_0))}{\dim(\mathcal{K}_\delta(\psi_0) \cup \mathcal{K}_\delta(\bar{\psi}_0))}, \quad (\text{S24})$$

which measures the overlap between numerical Krylov subspaces for  $|\psi_0\rangle$  and  $|\bar{\psi}_0\rangle$ .

The results are presented in Fig. S13(d). At  $\gamma = 2$ , long-time  $\eta$  between  $|\psi_{n_{\text{DW}}=L-2}\rangle$  and  $|\bar{\psi}_{n_{\text{DW}}=L-2}\rangle$  is close to  $\eta$  between two random pure states (indicated by dashed lines in Fig. S13(d)) regardless of the system size, which implies that they belong to the same Krylov subspace. In contrast,  $\eta$  between  $|\psi_{n_{\text{DW}}=2}\rangle$  and  $|\bar{\psi}_{n_{\text{DW}}=2}\rangle$  fails to reach the value between two random pure states even after a long time, and this discrepancy becomes more pronounced with increasing system size. Specially, for  $L = 12$ ,  $\eta$  remains almost zero for a long

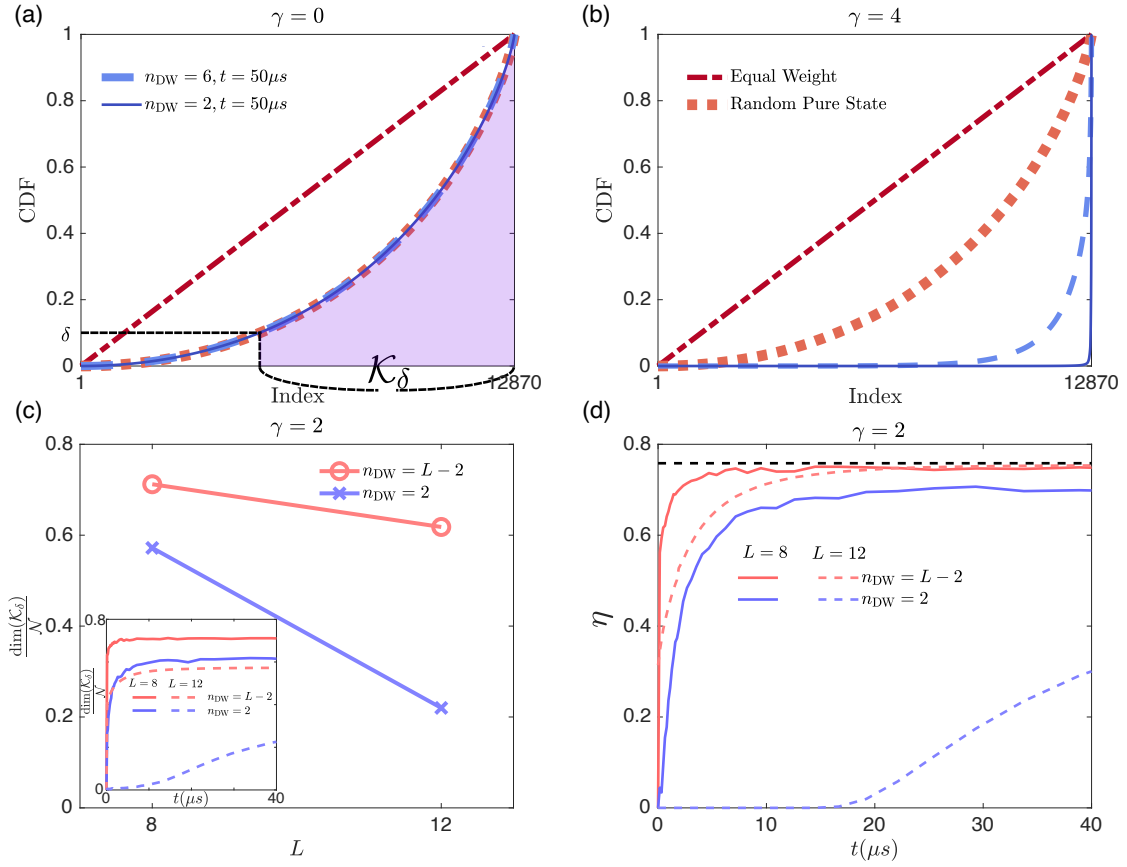


FIG. S13. **Numerical Krylov subspace in Stark systems.** (a), (b) The cumulative distribution function of the time-evolved states for  $|\psi_0\rangle = |\psi_{n_{\text{DW}}=2}\rangle$  and  $|\psi_{n_{\text{DW}}=6}\rangle$  at  $\gamma = 0$ , and 4. The cumulative distribution function for the state with equal weight on all the bases, and for a random pure state corresponding to the GUE are also provided for comparison. The shaded region in (a) corresponds to the bases which construct the numerical Krylov subspace. (c) The dimension of the numerical Krylov subspace for the initial states  $|\psi_{n_{\text{DW}}=2}\rangle$  and  $|\psi_{n_{\text{DW}}=L-2}\rangle$  with  $L = 8$  and 12 at  $\gamma = 2$ . The inset shows the time evolution of the dimension of  $\mathcal{K}_\delta(t)$  from  $t = 0$  to  $40\mu\text{s}$ . (d) The overlap between numerical Krylov subspaces  $\eta \equiv \frac{\dim(\mathcal{K}_\delta(\psi_0) \cap \mathcal{K}_\delta(\bar{\psi}_0))}{\dim(\mathcal{K}_\delta(\psi_0) \cup \mathcal{K}_\delta(\bar{\psi}_0))}$  for  $|\psi_0\rangle$  and  $|\bar{\psi}_0\rangle$ , with  $|\psi_0\rangle = |\psi_{n_{\text{DW}}=2}\rangle$  and  $|\bar{\psi}_0\rangle = |\psi_{n_{\text{DW}}=L-2}\rangle$ , respectively, and  $|\bar{\psi}_0\rangle = \prod_{j,m} \hat{\sigma}_{jm}^x |\psi_0\rangle$ . The dashed line denotes the typical value of the overlap between the subspaces corresponding to two random pure states.

time, and then slowly increase when  $t \gtrsim 20\mu\text{s}$  ( $\bar{J}_{\text{NN}}t \gtrsim 10^3$ ), which provides evidence that  $|\psi_{n_{\text{DW}}=2}\rangle$  and  $|\bar{\psi}_{n_{\text{DW}}=2}\rangle$  belong to different fragments, dynamically disconnected from each other. Note that the increase of  $\eta$  after  $t \gtrsim 20\mu\text{s}$  stems from the coupling of different fragments by higher-order terms in the perturbative expansion of Hamiltonian [Eq. (1)], which break the conservation of the emergent dipole moment and eventually leads to the destruction of fragmentation.

These findings raise intriguing questions of whether the subspace corresponding to  $|\psi_{n_{\text{DW}}=L-2}\rangle$  and  $|\bar{\psi}_{n_{\text{DW}}=L-2}\rangle$  will further fragment at higher  $\gamma$ , and whether there is a transition from weak to strong fragmentation [8, 9] with increasing  $\gamma$  in Stark systems. These questions requires a detailed investigation involving scaling analysis with respect to evolution time  $t$  and system length  $L$ , which is left for future exploration.

## TIME EVOLUTION WITH KRYLOV SPACE METHOD

In dealing with large systems, the full diagonalization becomes unfeasible. In our study involving up to 24 qubits, we employ the Krylov space method, which offers a more efficient approach for computing the time evolution of the system.

The unitary evolution of a isolated system governed by the Schrödinger equation can be expressed as

$$|\psi(t + \tau)\rangle = \exp(-i\tau\hat{H}/\hbar) |\psi(t)\rangle, \quad (\text{S25})$$

where  $|\psi(t)\rangle$  denotes the state at time  $t$ . The Krylov subspace of dimension  $m$  is spanned by the successive powers of  $H$  applied to  $|\psi(t)\rangle$

$$\mathcal{K}_m(\mathbf{H}, \mathbf{v}_0) = \text{Span}\{\mathbf{v}_0, \mathbf{H}\mathbf{v}_0, \mathbf{H}^2\mathbf{v}_0, \dots, \mathbf{H}^{m-1}\mathbf{v}_0\}, \quad (\text{S26})$$

with  $\mathbf{H}$  and  $\mathbf{v}_0$  being the matrix form of the Hamiltonian and the state, respectively. For Hermitian matrix  $\mathbf{H}$ , via

the Lanczos algorithm, an orthogonal transformation matrix  $\mathbf{K}_m = (\mathbf{v}_0 \ \mathbf{v}_1 \ \mathbf{v}_2 \ \dots \ \mathbf{v}_{m-1})$  can be constructed, which turns  $\mathbf{H}$  into a tridiagonal  $m \times m$  matrix form,

$$\mathbf{H}_m = \mathbf{K}_m^\dagger \mathbf{H} \mathbf{K}_m = \begin{pmatrix} \alpha_0 & \beta_1 & & & 0 \\ \beta_1 & \alpha_1 & \beta_2 & & \\ & \beta_2 & \alpha_2 & \ddots & \\ & & \ddots & \ddots & \beta_{m-1} \\ 0 & & & \beta_{m-1} & \alpha_{m-1} \end{pmatrix}. \quad (\text{S27})$$

Here,  $\alpha_j$ ,  $\beta_j$  and  $\mathbf{v}_j$  are determined by the Lanczos algorithm, which is an iterative procedure

$$\begin{aligned} \alpha_i &= \mathbf{v}_i \cdot \mathbf{H} \mathbf{v}_i, \\ \beta_i \mathbf{v}_{i+1} &= \mathbf{H} \mathbf{v}_i - \alpha_i \mathbf{v}_i - \beta_{i-1} \mathbf{v}_{i-1}. \end{aligned} \quad (\text{S28})$$

For a short time step  $\tau$ , the time evolution in S25 can be approximately calculated as

$$|\psi(t + \tau)\rangle \approx \mathbf{K}_m \exp(-i\tau \mathbf{H}_m / \hbar) \mathbf{K}_m^\dagger \mathbf{v}_0. \quad (\text{S29})$$

Given that the eigenvalues of  $\mathbf{H}_m$  are the most crucial  $m$  eigenvalues governing the dynamics at the current time  $t$ , the Krylov space method can yields highly accurate results. In this work, we adaptively select the time steps while ensuring convergence with  $m = 15$  Krylov vectors.

### POST-SELECTION OF MEASUREMENT RESULTS

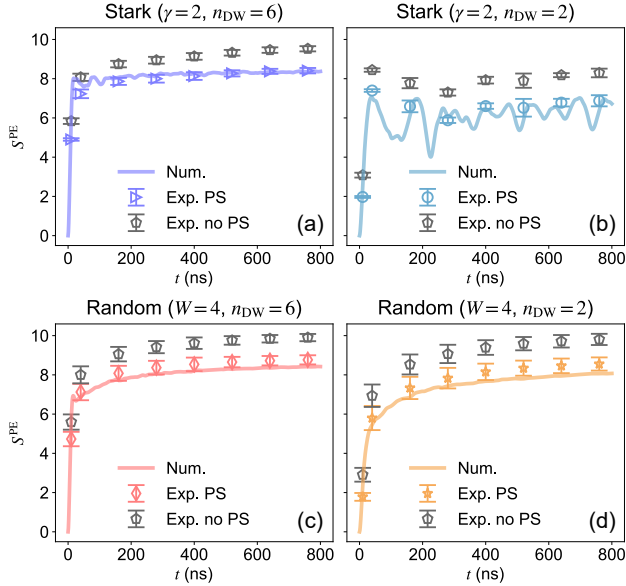


FIG. S14. **Effect of Post-Selection on Experimental Results.** The experimental data for the participation entropy (PE) with and without (grey data point) post-selection (PS) within the  $Q = L$  sector, in comparison with the numerical results (solid lines), for specific initial states in both Stark ( $\gamma = 2$ ) and random ( $W = 4$ ) potentials.

The Hamiltonian [Eq. (1)] in the main text conserves the total  $U(1)$  charge  $\hat{Q} \equiv \sum_{j,m} \hat{\sigma}_{jm}^+ \hat{\sigma}_{jm}^-$  during the time evolution. Despite the experimental evolution time being up to 800

ns, significantly less than the qubit energy relaxation times  $T_1 \sim 33.2 \mu\text{s}$  listed in Supplementary Tab. S1, the leakage out of the  $Q = L$  sector could still lead to an overestimation of the participation entropy (PE). To address this, we perform post-selection on the measured probabilities within the  $Q = L$  sector for the data presented in Fig. 4 in the main text.

Comparisons between the experimental results with and without post-selection, for  $\psi_{n_{\text{DW}}=2}$  and  $\psi_{n_{\text{DW}}=L-2}$  in a Stark and random potential, are depicted in Fig. S14. Notably, the inclusion of post-selection demonstrates a significantly improved agreement between the experimental and numerical results.

\* These authors contributed equally to this work.

† [huangkx@baqis.ac.cn](mailto:huangkx@baqis.ac.cn)

‡ [zcxiang@iphy.ac.cn](mailto:zcxiang@iphy.ac.cn)

§ [kaixu@iphy.ac.cn](mailto:kaixu@iphy.ac.cn)

¶ [hfan@iphy.ac.cn](mailto:hfan@iphy.ac.cn)

- [1] Y.-H. Shi, Z.-H. Sun, Y.-Y. Wang, Z.-A. Wang, Y.-R. Zhang, W.-G. Ma, H.-T. Liu, K. Zhao, J.-C. Song, G.-H. Liang, Z.-Y. Mei, J.-C. Zhang, H. Li, C.-T. Chen, X. Song, J. Wang, G. Xue, H. Yu, K. Huang, Z. Xiang, K. Xu, D. Zheng, and H. Fan, Probing spin hydrodynamics on a superconducting quantum simulator, [arXiv:2310.06565](https://arxiv.org/abs/2310.06565).
- [2] E. Torres-Herrera, J. Karp, M. Távora, and L. Santos, Realistic Many-Body Quantum Systems vs. Full Random Matrices: Static and Dynamical Properties, [Entropy](https://doi.org/10.1038/s41567-016-0186-1) **18**, 359 (2016).
- [3] S. Boixo, S. V. Isakov, V. N. Smelyanskiy, R. Babbush, N. Ding, Z. Jiang, M. J. Bremner, J. M. Martinis, and H. Neven, Characterizing quantum supremacy in near-term devices, [Nat. Phys.](https://doi.org/10.1038/nphys595) **14**, 595 (2018).
- [4] R. Nandkishore and D. A. Huse, Many-Body Localization and Thermalization in Quantum Statistical Mechanics, [Annu. Rev. Condens. Matter Phys.](https://doi.org/10.1146/annurev-conmatphys-060815-013848) **6**, 15 (2015).
- [5] D. A. Abanin, E. Altman, I. Bloch, and M. Serbyn, Colloquium : Many-body localization, thermalization, and entanglement, [Rev. Mod. Phys.](https://doi.org/10.1103/RevModPhys.91.021001) **91**, 021001 (2019).
- [6] S. Scherg, T. Kohlert, P. Sala, F. Pollmann, B. Hebbe Madhusudhana, I. Bloch, and M. Aidelsburger, Observing non-ergodicity due to kinetic constraints in tilted Fermi-Hubbard chains, [Nat. Commun.](https://doi.org/10.1038/s41467-021-24490-1) **12**, 4490 (2021).
- [7] Y. Yao, L. Xiang, Z. Guo, Z. Bao, Y.-f. Yang, Z. Song, H. Shi, X. Zhu, F. Jin, J. Chen, S. Xu, Z. Zhu, F. Shen, N. Wang, C. Zhang, Y. Wu, Y. Zou, P. Zhang, H. Li, Z. Wang, C. Song, C. Cheng, R. Mondaini, H. Wang, J. Q. You, S.-y. Zhu, L. Ying, and Q. Guo, Observation of many-body Fock space dynamics in two dimensions, [Nat. Phys.](https://doi.org/10.1038/s41567-023-01459-1) **19**, 1459 (2023).
- [8] S. R. Taylor, M. Schulz, F. Pollmann, and R. Moessner, Experimental probes of Stark many-body localization, [Phys. Rev. B](https://doi.org/10.1103/PhysRevB.102.054206) **102**, 054206 (2020).
- [9] P. Sala, T. Rakovszky, R. Verresen, M. Knap, and F. Pollmann, Ergodicity Breaking Arising from Hilbert Space Fragmentation in Dipole-Conserving Hamiltonians, [Phys. Rev. X](https://doi.org/10.1103/PhysRevX.10.011047) **10**, 011047 (2020).